UNIVERSITA' DEGLI STUDI DI PADOVA

Dipartimento di Ingegneria Industriale DII

Corso di Laurea Magistrale in Ingegneria Aerospaziale

DESIGN IMPROVEMENT AND ANALYSIS OF QUADRILATERAL MECHANISM LOCKS FOR MICROSATELLITE DOCKING SYSTEMS

Relatore: Branz Francesco

Ghedin Marco 1234058

Anno Accademico 2023/2024

Sommario

La rivoluzione dettata della New Space Economy ha portato a un aumento dell'impiego di micro- e nanosatelliti, grazie ai loro costi inferiori e i tempi di sviluppo delle missioni più rapidi. Negli ultimi anni, le interazioni tra spacecraft in termini di On Orbit Servicing, On Orbit Assembly e rimozione attiva di detriti hanno subito uno sviluppo notevole, diventando ambiti di crescente interesse sia per le potenzialità di estendere vita e funzionalità di spacecraft attualmente in orbita che per lo sviluppo di soluzioni innovative. Con il raggiungimento della maturità di queste tecnologie, scenari un tempo considerati eccessivamente complessi e svantaggiosi potrebbero tramutarsi in ordinari, rivoluzionando nuovamente l'approccio alla progettazione delle missioni.

In questo contesto, l'Università di Padova ha da sempre partecipato attivamente allo studio e sviluppo di soluzioni di docking, con un'attenzione particolare alla miniaturizzazione dei sistemi, come nel caso di DOCKS, il sistema di docking drogue-probe su cui questa tesi magistrale si concentra. In particolare, l'obiettivo principale di questo elaborato è di migliorare la parte di hard docking di DOCKS modificando il quadrilatero su cui si basa il meccanismo di bloccaggio a tripla tenaglia. Questo meccanismo svolge un ruolo cruciale nel garantire una connessione stabile e affidabile tra i due spacecraft.

Dopo una contestualizzazione del lavoro, evidenziando il ruolo trasformativo e l'importanza sempre più preponderante degli small satellites, vengono delineati gli obiettivi della tesi e il sistema viene quindi caratterizzato attraverso l'analisi cinematica e dinamica. Le modifiche proposte mirano a superare alcune limitazioni del sistema di docking preesistente, in particolare in termini di mantenimento del bloccaggio. Tenendo la compattezza ed efficienza fondamentali per missioni con satelliti di dimensioni così ridotte, è stata fatta una selezione di componenti per la realizzazione del meccanismo, con l'attenzione a minimizzare i consumi di potenza e l'ingombro, identificando tra questi anche gli attuatori da impiegare nelle future fasi di sviluppo del sistema di bloccaggio**.** Per affrontare scenari

in cui potrebbe verificarsi una mancata o incompleta apertura del sistema di bloccaggio, è stato sviluppato un meccanismo di rilascio, fornendo così un mezzo di protezione che consente lo sgancio completo dell'interfaccia drogue-probe. Il design del meccanismo di rilascio garantisce una separazione sicura e controllata, al fine di evitare danni allo spacecraft target.

I miglioramenti sono stati valutati attraverso simulazioni, evidenziando un incremento nelle prestazioni e una maggiore efficienza energetica per quanto riguarda il bloccaggio. Prospettive di sviluppo futuro del sistema prevedono miglioramenti in alcuni aspetti critici, quali l'ulteriore miniaturizzazione di alcuni componenti, un'ottimizzazione complessiva del meccanismo e lo svolgimento di test in laboratorio per validare i modelli matematici e le simulazioni.

Abstract

The rapid growth of the New Space Economy has led to an increased use of microsatellites and nanosatellites, due to their lower costs and faster development. In recent years interactions between spacecrafts in terms of on-orbit servicing, assembly and active debris removal have become appealing fields of interest furthering the expansion of existing space assets and development of novel solutions. Amid the growing interest in the subject over the last two decades, the University of Padova has actively participated in the study and development of docking solutions, including DOCKS, the drogue-probe docking system this thesis focuses on. Specifically, the primary objective of this work is to enhance the hard-docking part of DOCKS by introducing a redesigned quadrilateral mechanism with three locks. This mechanism plays a critical role in securing the docking interface, ensuring a stable and reliable connection between the two spacecrafts. After providing a comprehensive background on docking solutions in the introduction, highlighting the transformative role and growing importance of small satellites, the thesis objectives are outlined, and the system is characterized through kinematic and force analysis. The proposed redesign addresses key performance limitations of the existing drogue-probe docking system, particularly in terms of locking capabilities and resource utilization. It features adjusted dimensions and actuators selection to minimize its impact on the microsatellite's power consumption and weight constraints. To address scenarios where mechanism opening failure may occur, a release mechanism has been developed, providing a contingency measure by enabling the disengagement of the drogue-probe docking interface. The release mechanism's design ensures safe and controlled separation, preventing damage to the spacecraft or payloads. The enhancements have been evaluated through simulation, demonstrating significant improvements in docking performance and resource efficiency. Future research directions include improvements in some critical aspects, such as further miniaturization of some components, an overall optimization of the mechanism and testing.

Table of Contents

List of Figures

List of Tables

1. Introduction

1.1 Background and State of the Art

Since their first introduction in the early stages of the space era, satellites are increasingly playing a pivotal role in humanity development, becoming crucial in a spectrum of fields and fertile ground for research and development of new technologies. This transformative role of satellites is further exemplified by the emergence of the New Space Economy, which represents a significant shift in space exploration, characterized by increased involvement from private investors, companies, and startups. This transition marks a notable departure from the traditional government-centric approach to space initiatives, with the global space economy poised for rapid expansion, driven by the evolving nature of these investors and their investments.

A notable transformation is unfolding, propelled by the rise of small satellites, particularly in the categories of nanosatellite, weighing under 10 kg, and microsatellite, under the 100 kg. These compact solutions have ushered in a transformative era within the space industry due to their cost-effectiveness and rapid production capabilities [1]. In recent years, they have successfully assumed roles once exclusive to larger platforms: large constellations of small satellites are now effectively harnessed for Earth observation tasks [2], enabling endeavours such as climate change monitoring [3] and deforestation tracking [4], while in the realm of telecommunications they are starting to bring connectivity to both terrestrial and in-orbit domains [5]. Consequently, the traditional approach of costly and long-lasting satellites is shifting towards a continuous iteration and upgrading of assets.

This paradigm shift toward smaller and more versatile spacecraft also facilitates the development of novel satellite services tailored to the Internet of Things (IoT) [6] and Machine-to-Machine (M2M) communication [7]. These services capitalize on comprehensive and low-latency Earth coverage, underpinning the technological evolution.

The democratization of space and technology has paved the way for innovative mission opportunities. These encompass the growing interest in satellite-to-satellite interactions, exemplified by On-Orbit Servicing (OOS) [8] [9] [10] and the realization of larger structures through On-Orbit Assembly (OOA) [11] [12] [13] [14]. Notably, an emerging need for Active Debris Removal (ADR) [15] [16] is growing**.** The existing body of literature underscores numerous examples of these missions, predominantly grounded in CubeSats.

Executing these missions necessitates substantial technological advancements, particularly in the deployment and manoeuvring of small, autonomous spacecraft. To support these dynamic changes in the space market, key enabling technologies are essential in the field of navigation and guidance algorithms, micro-propulsion, vision/sensing, and telecommunications systems. All these advancements are pivotal in sustaining the pace of transformation in the space industry.

In the cited missions, autonomous capture and servicing solutions take on pivotal roles. Docking technologies are at the heart of these endeavours, as they enable the rigid connection between spacecrafts. Moreover, there is a growing trend towards downscaled missions for technology demonstration purposes. Demonstrating docking capabilities between miniature autonomous vehicles has proven to be highly valuable from both cost and risk perspectives. Notably, the interest in docking technologies for small satellites is a relatively recent development, with significant advancements dating back to the early 2000s [17], [18], [19] [20], [21] [22], [23] [24]. This evolution underscores the increasing importance and relevance of docking systems in the context of small satellites, aligning with the core focus of this thesis.

1.2 Thesis Objectives

The primary objective of this thesis is to enhance an existing drogue-probe docking system for small satellites, which is currently under development at the University of Padova [25]. The improvements aim to address specific challenges associated with the current design of the locking mechanism while optimizing its performances. The following objectives outline the key areas of focus for this research:

1. **Comprehensive System Understanding:** The initial step involves a thorough understanding of the existing drogue-probe docking system. This includes the study of its design, components, and operational principles. The objective is to gain in-depth knowledge of the system's characteristics and limitations.
2. **Component Selection:** In parallel with the understanding of the existing system, the research will involve the selection and analysis of motors, joints and springs to transition from the conceptual design to the limits of the practical implementation.
3. **Alternative Configuration Development:** Building on the insights gained from the first evaluation and the available components, the thesis will delve into the development of an alternative configuration for the four-bar linkage mechanism. This alternative design will seek to address the identified challenges and offer enhancements in terms of performance and reliability.
4. **Kinematic Analysis for Characterization:** The research will conduct a comprehensive kinematic analysis of the existing and proposed docking system. This analysis will involve a detailed examination of the system's motion, trajectories, and geometric properties. By characterizing the system kinematically, the aim is to gain a deeper understanding of its behaviours during the docking process.
5. **Force Analysis for Performance Evaluation:** With a solid grasp of the system's kinematics and the components in use, the research will delve into the

dynamics of the drogue-probe docking system. This analysis will focus on the forces, torques, and mechanical behaviours during the docking operation. Understanding the dynamics is crucial for optimizing the system's performance while ensuring reliable and precise docking.

6. **Release Mechanism Design:** As an integral part of the research, a release mechanism will be designed to address scenarios where the system fails to release the drogue.
7. **Critical Aspects Assessment:** The alternative configuration will be subjected to a comprehensive assessment to measure its effectiveness in improving the system's performance. Even after the improvement, some challenges or areas for future enhancement may persist. This objective is to identify and document these remaining challenges, laying the groundwork for potential future work.

1.3 Thesis Structure

After establishing the objectives of this work, the structure of the thesis adheres to the following framework:

Chapter 2: *Overview on Docking Solutions*

- This chapter lays the foundation for the study by categorizing existing solutions and describing the different phases of typical docking operations, highlighting critical aspects involved.

Chapter 3: *Initial Design Analysis and Component Selection*

- In this chapter, the initial design of the drogue-probe docking system is described in detail and the process of components selection is presented, considering environmental, spatial and power constraints.

Chapter 4: *Kinematic and Dynamic Analysis*

- This chapter explores the kinematic and force analysis of the proposed docking system, to have a better characterization of the mechanism and evaluate the feasibility of the new solution. The groundwork is laid for the following chapter.

Chapter 5: *Configuration Evolution*

- In this chapter the configuration for the quadrilateral mechanism is developed in detail, as a direct consequence of the identified critical aspects emerged in *Chapter 3* and with the aid of the analysis conducted in *Chapter 4.*

Chapter 6: *Release Mechanism for Drogue Ejection*

- In this chapter, the development of a release mechanism will be detailed, providing a failsafe option for unlocking the docking system.

Chapter 7: *Discussion of Results and Comprehensive Assessment*

- In this chapter, a comprehensive assessment of the developed configuration's performance is conducted. It also discusses potential issues and identifies and documents remaining challenges.

Chapter 8: *Conclusion and Future Work*

- The final chapter summarizes the key findings and their implications, providing directions for further enhancing the system.

2. Overview on Docking Solutions

2.1 Evolution of Docking

The development of spacecraft docking capability hinged on space rendezvous, the art of two spacecraft locating each other and maintaining the same orbit. In-space rendezvous and joining of two bodies was one of the first technological challenges that space engineers dealt with. Since the first docking of two spacecraft during Project Gemini, under the command of Neil Armstrong (1966), active joining of two or more bodies radically changed and evolved in different concepts of operations. Two years after those first manual docking operations, the Soviet Union started adopting automated systems and performed the first docking between two unmanned vehicles: Kosmos 186 and Kosmos 188. As a direct product of these first steps, docking has lately found a place in the realm of small satellites, as depicted in the introduction in *Chapter 1*.

2.1.2 Phases of Docking

Usually, the approaching spacecraft is named *chaser*, and the approached body is referred to as *target*. Within this nomenclature, the classification of main joining operations can be based on mission target attributes: if the target is passive, as it happens with an uncooperative spacecraft or space debris, the chaser approaches and captures it, usually without the presence of joining interfaces or other useful grasping elements. Tumbling motion of the target is a common issue of this operation; in the case of cooperative bodies, there is further classification: *berthing* is an assisted joining which needs the help of a grapple interface (such as ISS robotic arms) to bring one spacecraft and mate it to the other module. On the other hand, *docking* is the direct active mating of two separate free-flying spacecraft through active proximity manoeuvres.

Docking itself involves three distinct phases, each contributing to the successful connection between the two vehicles:

1. **Approach Phase:** This initial phase involves the chaser, carefully manoeuvring toward the target, closing the distance while maintaining precise alignment. This phase is crucial for ensuring a safe and controlled approach.
2. **Contact and Capture Phase:** In this phase, the chaser makes physical contact with the target satellite, capturing it. A variety of elements, such as docking probes, magnets, or capture latches, could be involved to secure the connection.
3. **Locking Phase:** After capture, the chaser proceeds to fully dock with the target. This phase involves eliminating any remaining relative motion between the two satellites, establishing a rigid connection.

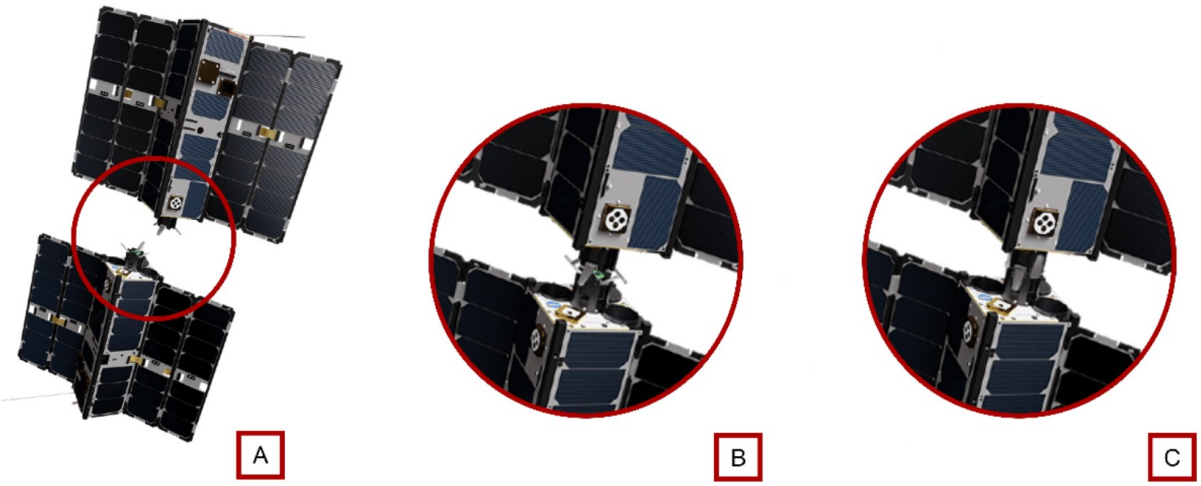

Figure 1: phases of docking based on CPOD mission [26] (A: Approach Phase; B: Contact and Capture; C: Locking Phase)

A docking connection can be referred to as either *soft* or *hard*. Typically, a spacecraft initiates a soft dock during capture, allowing some degree of flexibility in the connection. In hard docking, the mating interfaces are further engaged to create a

firm and often rigid connection between the two spacecraft, enabling the exchange of payloads, data, or other mission-specific tasks.

2.2 Classification of Docking Types

Based on the mating interfaces and strategies to perform docking operations, these categories can be identified:

1. **Probe–Drogue Systems:** These are the simplest and most common types of docking systems. They consist of a probe that extends from one spacecraft and a drogue that is placed on the other spacecraft, as presented in Examples are presented in the first scheme in *Figure 2*, referred to the apollo missions. When the probe and drogue mate together, they create a rigid connection between the two spacecraft. This configuration is widely used in docking operations involving spacecraft with different sizes and purposes. In this setup, the larger spacecraft usually carries the drogue, while the smaller one has the probe. In the field of autonomous docking between microsatellites, two examples of this are The Michigan Aerospace Autonomous Microsatellite Docking System prototype [27] and the one in the framework of the ARCADE student project developed at the University of Padova [23].
2. **Androgynous Docking Systems:** In these systems, docking ports on both spacecraft have the same shape and functionality, as shown in the second example in *Figure 2*, offering system-level redundancy and great flexibility in mission design, as either spacecraft can dock with the other. This type of solution is well-suited for scenarios involving multiple spacecraft with interchangeable roles and in OOA operations, but it can be also critical in rescue missions. A great example of application of this type of docking solution is the Universal Docking Port (UDP) featured in the SPHERES project (Massachusetts Institute of Technology) [28] which represented a milestone in the advancement of small satellite autonomous rendezvous and docking

manoeuvres and more recently, the CubeSat Proximity Operations Demonstration (CPOD) project developed an androgynous docking interface for 3 U CubeSats [26].

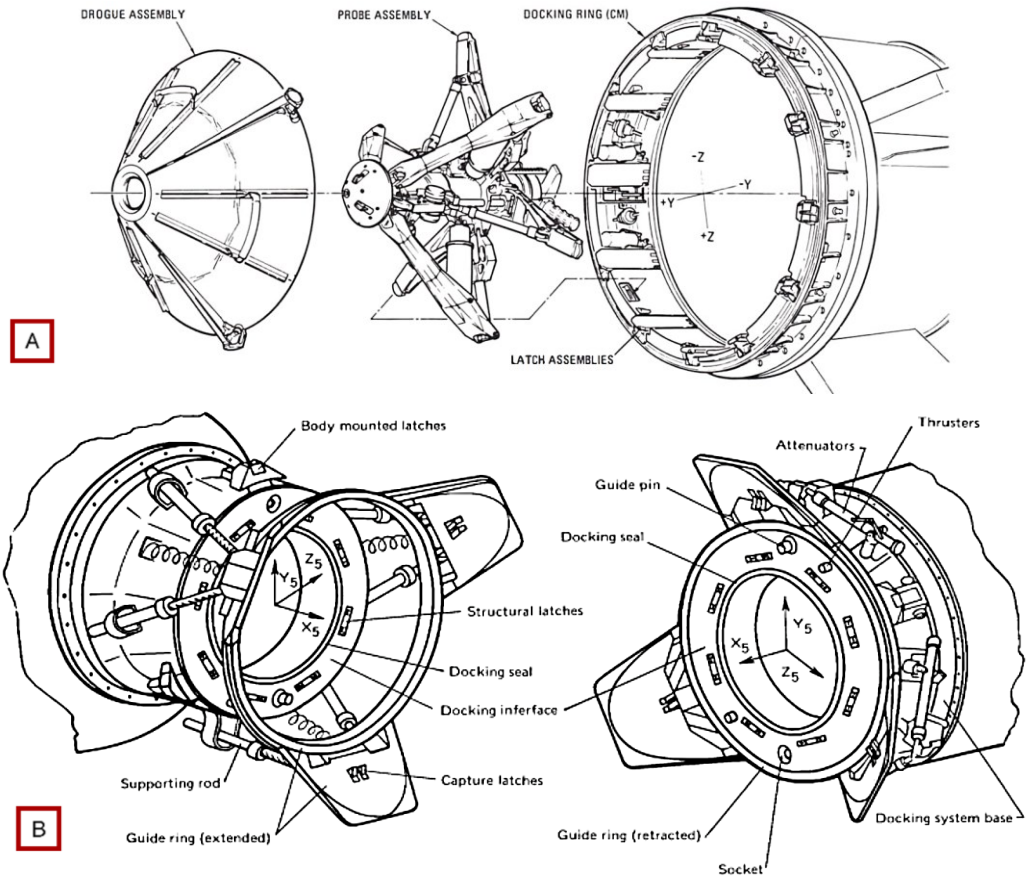

Figure 2: examples of docking interfaces (A: drogue and probe of Apollo mission [29]; B: androgynous docking system of ASTP mission [30])

In addition to these two main categories, solutions based on magnetic docking have been investigated in recent years and demonstrated to be valuable for both soft docking and proximity operations between small satellites. These solutions are either used as standalone as in [31] and [13] or combined with mechanical hard docking as in [32] [13] and in the solution considered in this thesis.

2.3 Challenges of Docking for Small Satellites Solutions

The diversity in proposed miniaturized solutions available in the literature arises from the distinct challenges posed by docking small satellites, needing robustness to uncertain parameters, and minimization of safety risks, while allowing the spacecrafts to operate autonomously. Designing docking systems for small satellites presents a unique set of challenges, notably spatial constraints due to the compact nature of these spacecraft. Additionally, limited resources, particularly in terms of available power and propulsion capabilities, pose critical challenges. Therefore, managing rendezvous and docking manoeuvres becomes complex, demanding optimization of each component for efficiency. Undesired dynamics or damages may result from strong impulsive forces and torques during contact, emphasizing the need for robust satellite Guidance, Navigation, and Control (GNC) in addition to the aforementioned efficient propulsion systems. Adopting docking interfaces capable of mitigating hard contact effects enhances overall robustness, contributing to mission safety.

3. Initial Design Analysis and Component Selection

The initial design of the docking system on which this thesis is based is DOCKS, a solution provided by the Department of Industrial Engineering of the University of Padova for use onboard micro- and nanosatellites [25], developed in the framework of the future ESA mission SROC (Space Rider Observer Cube) [33].

3.1 SROC mission

This mission is a European Space Agency technological demonstrator made in partnership with a consortium of Italian industries and institutions including Polytechnic of Turin, University of Padua, Tyvak International and StellarProject SRL with the main purpose of performing proximity operations, docking and undocking with the Space Rider (SR), which is a new uncrewed space laboratory, transport system and re-entry vehicle developed for ESA by Thales-Alenia [34].

Following the mission outline presented in *Figure 3* [35], the 12U CubeSat SROC, namely the chaser, will be deployed (DEP) from the target SR's cargo bay at an altitude of 400 km and after performing Early Phase Operations (EOP) and reaching proper distance with respect to SR during Rendezvous Phase (RVP), it starts to perform multispectral camera observation runs in closed proximity of SR during the SR Observation Phase (SROP), followed by a Docking and Mating Phase (DMP) for retrieval inside the cargo bay of SR. After successfully docking, the CubeSat will re-enter the Earth's atmosphere alongside SR, with the overall mission completed (EOL) paving the way for future advancements in recurring satellite servicing missions.

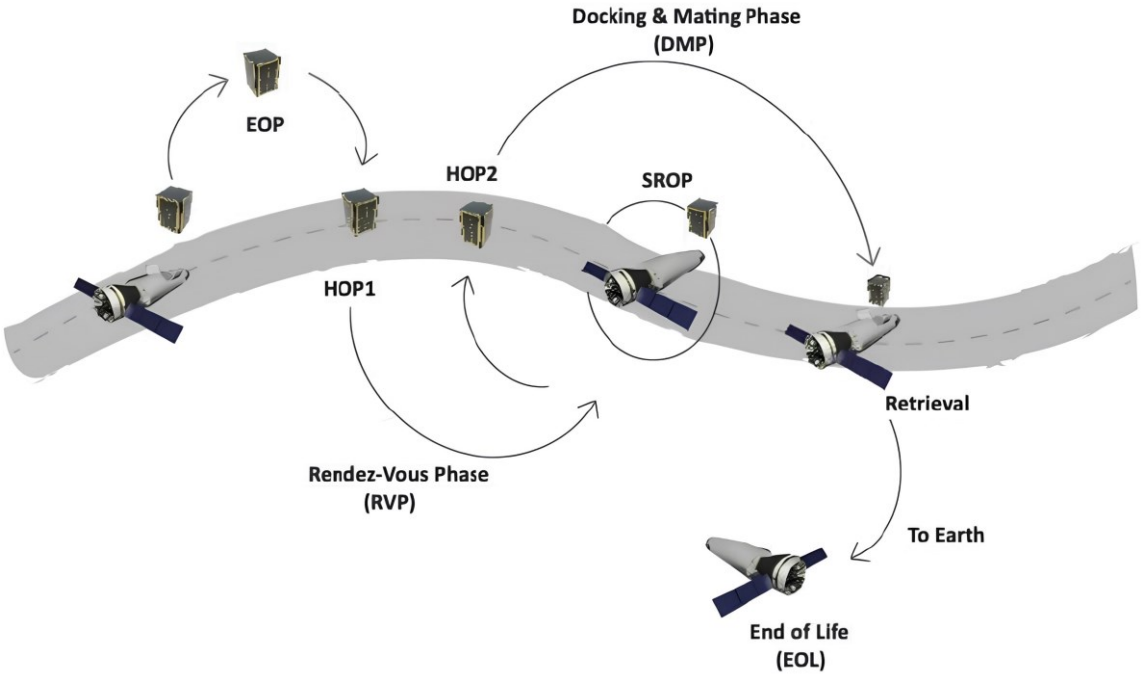

Figure 3: SROC mission phases. HOP1 and HOP2 are Hold Point Phases meant to stabilize the transition between two distinct phases, obtained from [35].

3.2 DOCKS

The system combines a classical probe-drogue configuration with a soft docking electro-magnet and three locking claws to perform the rigid connection between the probe and the drogue. A set of navigation sensors and a dedicated computer are also incorporated to estimate the attitude and relative position of the target autonomously, making it a smart standalone solution. The system components of the chaser and the target are presented on the left and right sides of *Figure 4*.

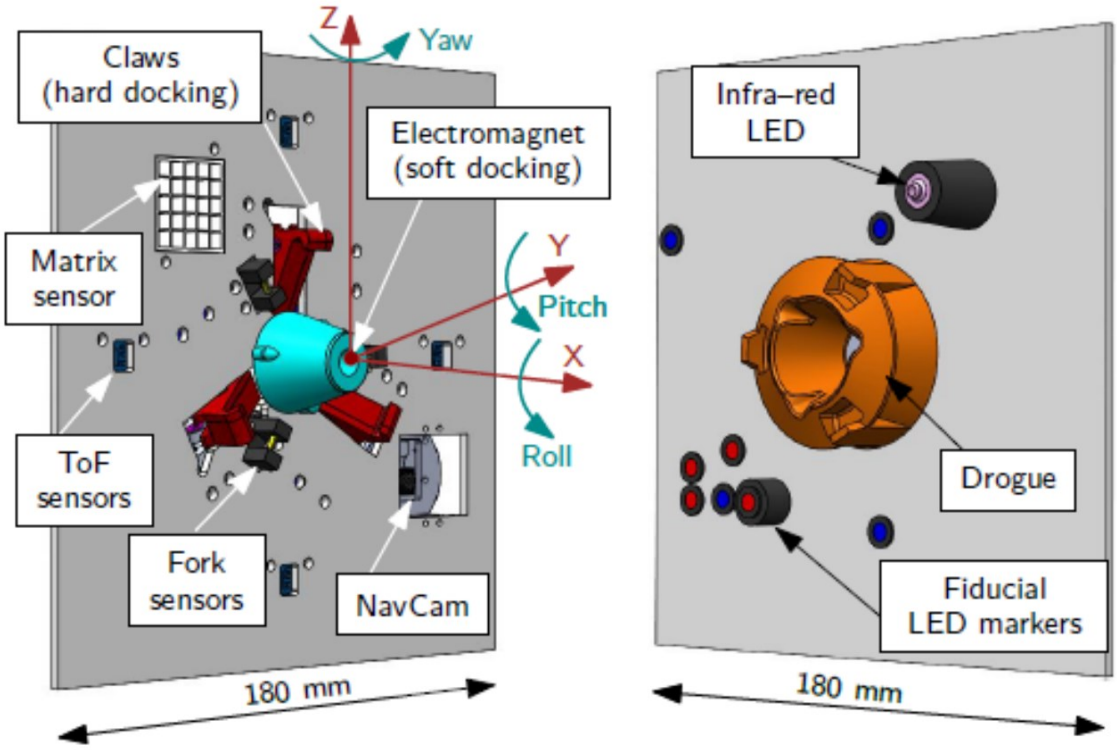

Figure 4: description of the system components of the initial design, obtained from [25].

Proceeding with a more detailed description, the chaser, holds the active part of the docking system, making use of two main elements: a centring cone-shaped probe containing an electromagnet for the soft docking and around it, angularly spaced by 120°, three motor-actuated four-bar linkage claws to perform the hard docking. To measure the relative position between the chaser and the target, on the external plate of the chaser are also included the following sensors: a navigation camera to measure the relative pose between the two spacecrafts by recognising the LED pattern on the target at distances with a range of 1m down to 50 mm; four Time of Flight sensors to measure both distance and relative pitch and yaw angles from 100mm up to contact; a phototransistors matrix sensor to measure relative position in the axis perpendicular to the docking direction, receiving the light cone generated by an infrared LED placed on the target.

The target instead features a passive drogue with a mating interface to force the alignment with the probe and an external ring-shaped grappling fixture to be locked in place by the claws. At the base of the drogue is located a ferromagnetic plate to couple with the electromagnet inside the probe. The drogue is connected to the frame of the chaser through a damper, which has been included to soften the impact with the chaser during capture and reduce oscillations during the whole docking operation. To complete the set of docking elements, three fork sensors are placed on the chaser, alternating with the claws around the base of the probe to match with three respective protruding features on top of the drogue of the target. Their purpose is to provide the activation signal to the claws and act as acknowledgement for the soft docking.

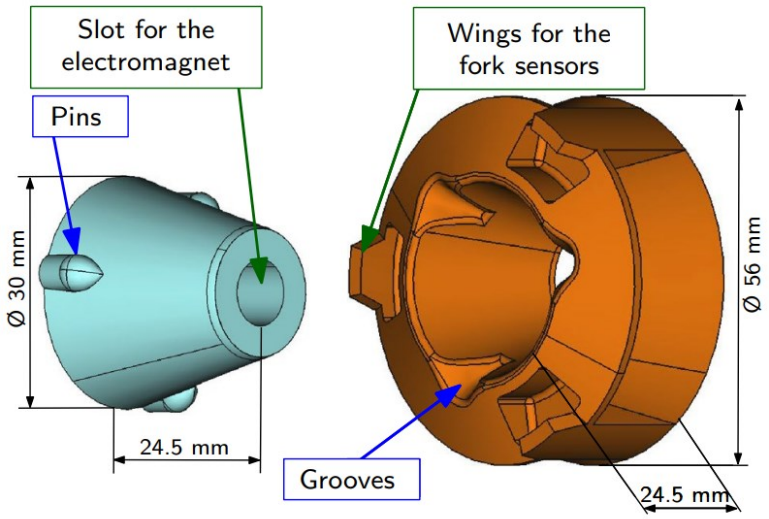

Figure 5: probe and drogue design, obtained from [25].

After the approach phase, in which most of the alignment is obtained, contact and capture is performed through the action of the electromagnet inside the probe, which couples with the ferromagnetic plate of the drogue. The probe-drogue magnetic interaction proceeds guided by the conical shape of the probe and its corresponding on the drogue, which allow for a 10° of pitch and yaw misalignment and

10mm of lateral misalignment. To force the roll alignment, the rim of the probe includes three protruding pins, which mates with the grooves on top of the drogue ad highlighted in *Figure 6.* At the same time, other three features protruding from the drogue cover the aforementioned optical fork sensors around the probe, signalling that the locking distance is reached. When capture is completed, the four-bar linkages are actuated and the tips of the three claws close around the drogue rim to rigidly lock the connection between the two spacecrafts as showed in *Figure 7*.

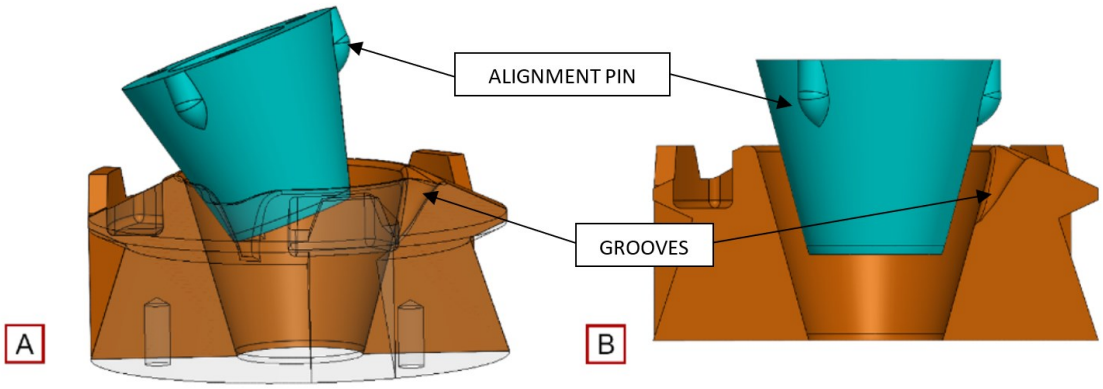

Figure 6: DOCKS self-alignment capabilities (A: angular alignments; B: roll and in-plane alignments)

The quadrilateral mechanism is composed of these four components: two links of 10mm length, one of which is connected to the motor shaft, the frame support with two holes for the bearings spaced 20mm and the claw, which hosts other two bearing holes spaced 20mm, as shown in *Figure 7*. The probe and drogue protrude from the host spacecraft external surfaces by 24.5 mm, while their external diameters are 38 mm and 56 mm respectively, while the maximum aperture of the claws is set to 29.6mm measured from the claw tip to the centre of the probe. These dimensions are compatible with the CubeSat standard if the docking interfaces are mounted on either (top or bottom) of the CubeSat bases, a key point for standardizing the interface.

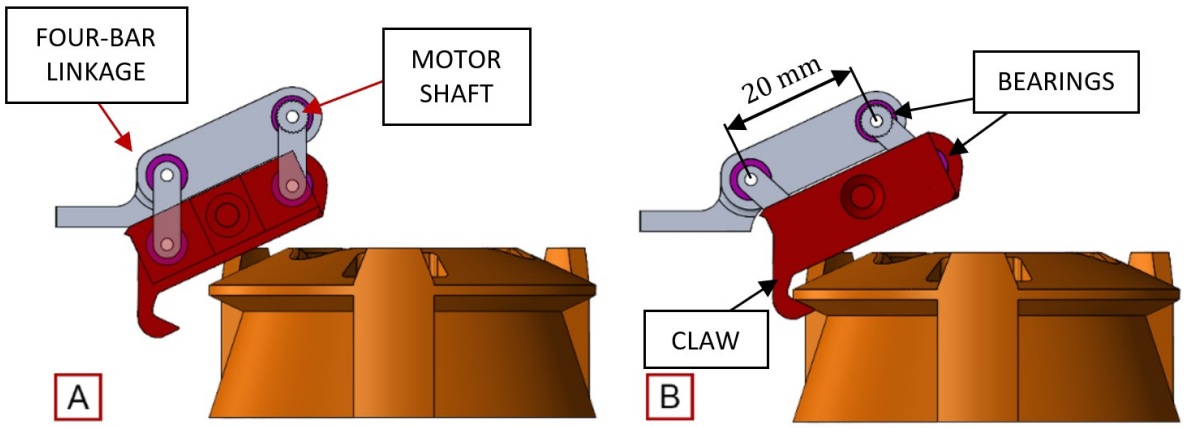

Figure 7: drogue-claw interaction (A: mechanism fully opened; B: mechanism closed)

To gain insights into the masses involved, a laboratory prototype was manufactured for preceding investigations, based predominantly on plastic materials for most components. The motion transmission elements and supports, however, were machined in aluminium. The probe, inclusive of sensors and actuator, weighs 51 g, while the drogue has a mass of 17 g, resulting in a total mass of 68 g. These mass values only partially reflect a potential future flight model, which would probably be manufactured mainly in aluminium. Considering the mass densities of the two materials and factoring in mass-oriented optimizations, the estimated total mass of the flight version of the docking mechanism is estimated to be below 150 g.

3.3 Components Requirements and Selection

In the described design, the active components of the docking mechanism are located on the target, the smaller spacecraft with limited resources and space, already densely populated by sensors and other components in the docking area. While the electromagnet and other components had already been chosen or were in development at the beginning of this study, some crucial components were still missing. Therefore, time was dedicated to the analysis of available off-the-shelf

motors and joints, searching for the ones that could fulfil the constraints. For the sake of compactness of the whole docking solution it was necessary to choose the lightest, smallest, and most energy-efficient components. Due to the space environment in which the system must operate, temperature and vacuum compliance are mandatory specifications to meet. During this early stage of development, to minimize costs while ensuring that mechanical performance remains equivalent to the final system, the search focused on components with an existing variant or a very similar counterpart that is space-qualified or vacuum-compliant to be purchased only after design and test a prototype of the docking mechanism using the non-qualified available components. Once the prototype is functional, the equivalent components can be purchased for space environmental tests and further development to ensure that it meets all the requirements.

As for requirements, the motor was set to:

- operate within a maximum 5W power each, for a total of 15W
- be compatible for standard voltages such as 3.3V, 5V, or 12V

Furthermore, the allowed area for the entire docking system has a diameter of 16cm and is filled with other components, such as the optical forks and ToF sensors, so the candidate motor had to be lightweight and compact, defining other two requirements:

- weight under 0.1kg
- have dimensions smaller than 40mm envelope and 45mm length

A minimum torque was then set at 6 mNm to complete the motor requirements.

As a result of the search, the *Table 1* presents the list of vacuum-compliant motors that fitted one or more of the abovementioned requirements. Within this list, only Faulhaber had some models respecting most of the requirements, while only two of them were fulfilling them completely, so the choice was about the most perfor-

mant in terms of torque. Apart from fulfilling all of the requirements, some considerations can be made from the analysis of *Table 1*: it can be observed that some motors have the capability to produce a significantly higher torque than the chosen motor, such as in the case of Faulhaber's AM3248, or they exhibit a lower angular step. However, one of the key criteria was to focus on selecting motors as compact as possible, aiming to minimize the impact in terms of power, mass, and volume. Only as a second step of evaluation, attention was directed towards the generated torque and angular resolution. For these reasons, motors such as the phyBASIC 20-1 or phyBASIC 28-1, despite their compact size, were set aside due to their excessive power consumption. Given that the case of application involves a straightforward actuation of the linkage and considering the objective of not involving the motor in maintaining the lock after the closure actuation, it was not a priority to select a motor with a very small angular step or extremely high torque.

Model	Manufacturer	Size (mm)	Length (mm)	Angle (°)	Mass (kg)	Volt (V)	Current (A)	Power (W)	Hold Torque (mNm)
DM0620	Faulhaber	6	9.5	18	0.0011	3	0.08	0.25	0.25
AM2224	Faulhaber	22	27.7	15	0.043	3	0.5	1.5	22
DM40100R	Faulhaber	40	25.6	3.6	0.125	24	1.32	63.12	62
AM3248	Faulhaber	32	42	7.5	0.160	12	0.7	8.4	85
phyBASIC 20-1	phyTRON	20.1	31.5	1.8	0.050	48	0.6	28.8	16
phyBASIC 28-1	phyTRON	28.3	31	1.8	0.100	48	1	48	65
phyBASIC 42-1	phyTRON	42.3	34.3	1.8	0.210	48	1.5	72	320
ZSS Standard 26.200.0.6	phyTRON	25	47	1.8	0.110	70	0.67	46.9	25
phySPACE 32-2	phyTRON	33	48	1.8	0.211	48	0.6, 1.2	28.8	50
phySPACE 25-2	phyTRON	26	36	1.8	0.100	48	0.6, 1.2	28.8	13

Table 1: list of motors

The selected one, AM2224, boasts a compact size with a 22mm envelope, a length of 27.7mm (34.6mm including the shaft), a weight of 0.043kg, and a power rating

of 1.5W. Crucially, it provides a holding torque of 22 mNm. The motor's step angle of 15° initially raised concerns, as finer control was desired. To address this, a 3.75:1 reducer was considered to reduce the step angle to 4°, enabling more precise rotational control. However, the desire for a compact design led to the postponement of the reducer's inclusion. The potential for future inclusion exists, especially if increased torque becomes a necessity, but complicates the integration in the already dense design. As Faulhaber provides an encoder for the selected stepper motor, it was included to enable micro-stepping and enhance control, mitigating the immediate need for further precision enhancement. With the addition of the encoder PE22-120, the total length of the actuator results in 38mm, remaining under 45mm.

A second aspect to be considered in the component selection is the type of joints, being pivotal elements in the mechanism's reliability, and affecting the overall motion. Working with miniaturized parts like the ones in the four-bar linkages, the joints had to be particularly small and reliable.

A first hypothesis was to consider the implementation of flexures, making the four-bar linkage a compliant mechanism. Transitioning from a traditional rigid-body mechanism to a compliant mechanism offers advantages like removing sliding contact between surfaces, monolithic manufacturing, higher precision, reduced friction, and reduced weight [36]. Despite facilitating smooth, continuous motion, without backlash, and with high levels of repeatability and precision, compliant systems have some drawbacks owing to their intrinsic coupling of kinematics and elastomechanical behaviours. Consequently, design and analysis cannot be done by separating kinematics and dynamics. The design process is even more complicated if the compliant elements undergo large deflections, such as in the considered case of application, due to the resulting nonlinear relationship between stress and strain with the angular deflection of flexures constrained by these values, limiting the motion range of the mechanism, and introducing challenges in achieving precise relative rotation [37].

The considered choice was then to keep using ball bearings with an external diameter of 6mm, inner one of 2mm and width of 3mm, as in the original design. Even though this means working with particularly small joints, after checking for the availability of the components in manufacturers, given the loads that the mechanism is expected to withstand, the choice seemed reasonable. Having such small ball bearings allows more freedom in the redesign of the four links, having the possibility to both keep the design slim and further shrink components, while avoiding making the whole linkage weaker and more prone to breakages than the original one.

In both motors and joints, as both involve ball bearings, particular attention was posed to the lubricant choice to avoid outgassing and drop in performance in the harshness of space. To avoid leakages contaminating the various sensors in the nearby of the four-bar linkages, preferences were given to solid lubricants giving better vacuum stability. As an alternative, High Vacuum Greases as the Braycote 601EF can be used while keeping the outgassing and consequent contamination to TML < 1.0 %, and CVCM < 0.1 %, as per ASTM E595 guidelines. Having the mechanism joints perform only portions of a complete rotation and for a limited amount of time, reducing friction to the minimum was not fundamental in terms of longevity of the system, but useful in reducing the energy dissipation and avoiding solicitations during actuation.

3.4 Analysis of Critical Issues

The initial design of the docking system presented some critical aspects that could be improved, specifically concerning the locking capabilities of the claws. Considered hard docking components, the claws come into action when the two spacecraft have already reached the minimum distance and most of the relative motion has been eliminated through soft docking and attitude control of the chaser. Consequently, the forces that the claws must counterbalance are minimal and can be

easily overcome through the actuation of the motors. However, this implies that the actuation must remain implemented throughout the entire time the two spacecraft remain docked, resulting in continuous power consumption.

A change of strategy for the locking system was therefore considered necessary. In particular, the operating principle of the motor-actuated quadrilateral was kept, but it was decided to change how the quadrilateral locks itself around the drogue, allowing a passive keeping of the locking position for an indefinite time.

3.5 Nomenclature and Reference Systems

Given the central symmetry of the system, to reduce complexity, the focus was placed on the in-plane behaviours of a single quadrilateral, taking respectively the external plate of the chaser and the opposite of the docking direction as the horizontal and vertical axes of the system of reference centred in the motor link *A* as represented in blue in *Figure 8*. From here on, the quadrilateral components will be considered as follows: *AB* is the input link connected at one end to the motor and at the other to the claw, *CD* is the output link, the second rod that connects the claw to the frame, *DA* is the distance between the two frame links and *BC* is the distance on the claw between the joint with *AB* and the joint with *CD*. Point *T* stands for the claw tip, the protruding part of the claw that makes contact with the drogue. During the position and forces analysis a second reference system has been introduced, parallel to the first one, but centred in the point *T* at the end of the motion, presented in red in *Figure 8*.

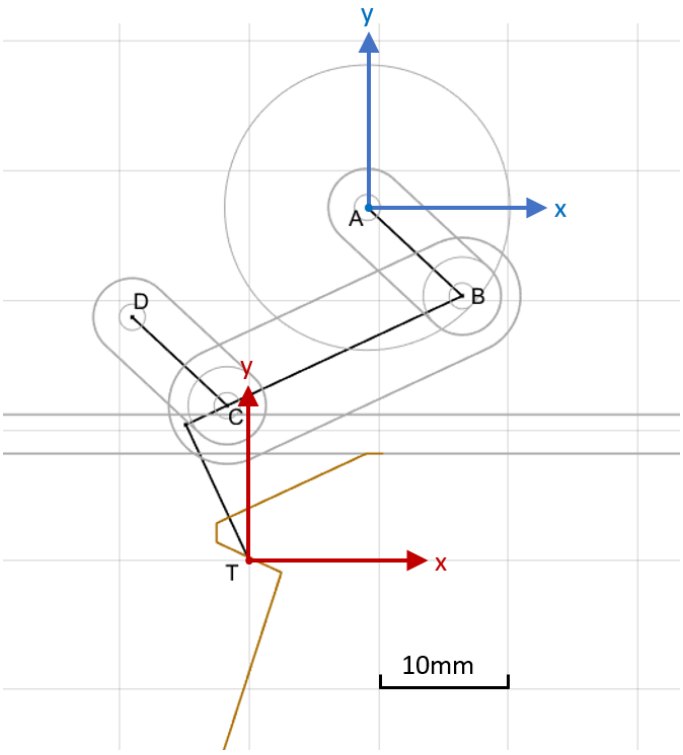

Figure 8: systems of references used in the thesis.

3.6 First Motion Studies

For a better understanding of the physics, the system was modelled in 2D using the Working Model 2D simulator. Starting from the original mechanism configuration, motion studies were performed by varying the dimensions of the four components to obtain a preliminary draft of the alternative closure. With the main goal to obtain a configuration that keeps the mechanism locked even in the presence of external forces pulling the drogue, the most fitting solution considered the introduction of an extra-rotation to the input link *AB* with respect to the docking direction axis, to abut the mechanism against the frame. In this scenario, a solicitation on the tip of the claw opposite to the docking direction that would have the effect of moving the linkage along its trajectory is counteracted by *AB* already abutting the frame, so no further motion is possible in that direction. The link *AB* can be abutted in both directions of motor rotation, but considering a constant velocity

delivered by the motor, the counterclockwise rotation was chosen as it produced more gradual movements near the mechanism closure, ensuring better control and a rotation consistent with that of the claw, while the clockwise direction had the claw rotating in the opposite direction of the link *AB*. The counterclockwise solution also provided a wider range of motion, offering greater freedom of action in the subsequent work phases.

To swiftly visualize the mechanism and its range of motion and make rapid adjustments to sizes and positioning on the satellite plate, GeoGebra has been employed extensively, because well-suited for exploring and interacting with geometrical models parametrically, providing a quick and efficient means of assessing the design.

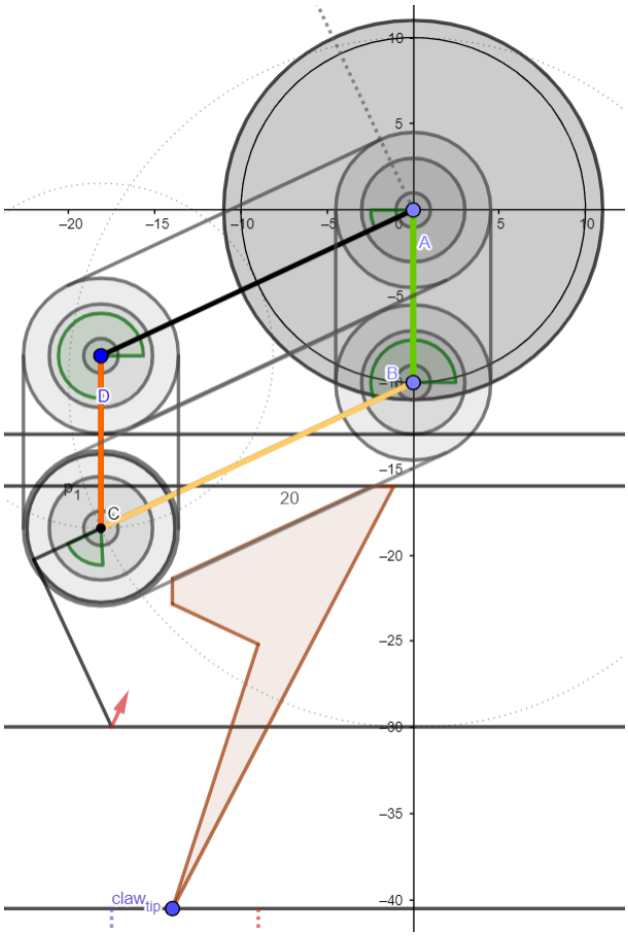

Figure 9: GeoGebra geometrical model of the original mechanism.

Afterwards, SolidWorks was utilized for the detailed modelling of the final components and for tailoring these components to seamlessly integrate into the complete assembly. The combination of GeoGebra and SolidWorks facilitated both the conceptual understanding of the 2D mechanism properties and behaviours and the practical implementation of the whole design in the three-dimensional space. Throughout the development, both MATLAB and Working Model 2D helped in the mathematical modelling and understanding of the mechanism.

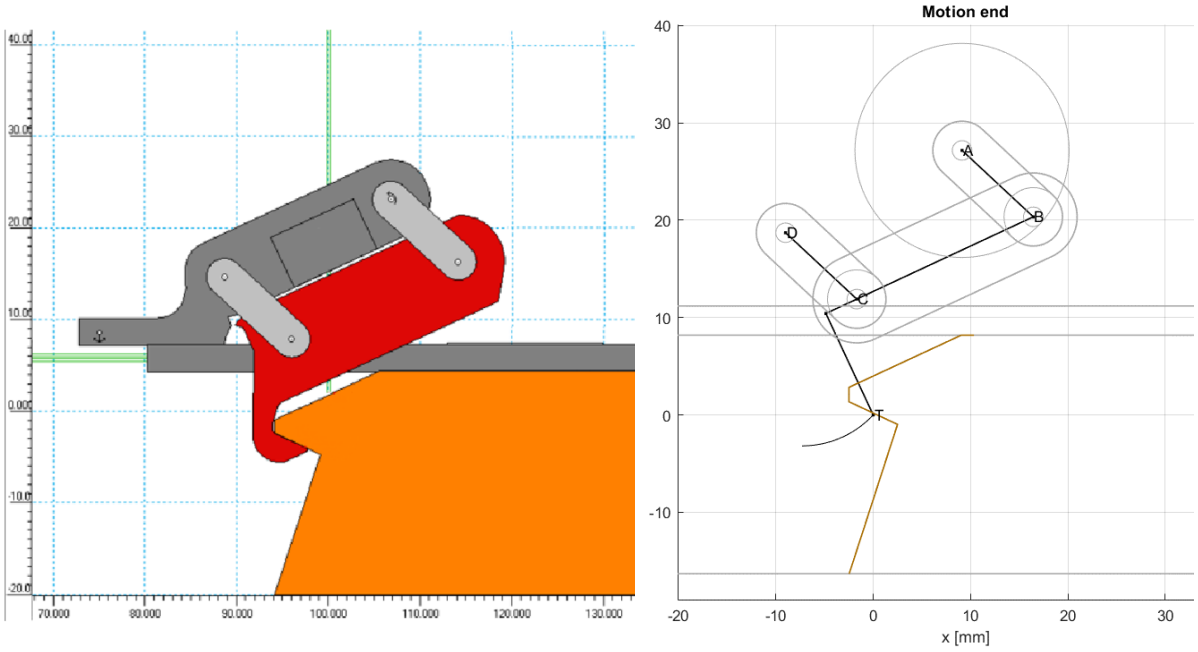

Figure 10: Working Model and MATLAB models

4. Kinematic and Dynamic Analysis

To better characterize the system, a kinematic analysis was conducted on the quadrilateral, following a further abstraction process that considered only the characteristic elements of the system: the position of the claw tip T, the distance between joints, which were considered point-shaped ideal rotational couplings, and the orientation of the quadrilateral with respect to the reference system mentioned in the previous chapter.

4.1 Recalls of Applied Mechanics

Considering the mechanism as a planar quadrilateral, with four rigid bars, here are presented some key concepts.

The number of degrees of freedom is the number of free coordinates needed to define the position of a mechanism. Considering the planar case directly, it is possible to write the structural equation, or Grubler's equation, for calculating the degrees of freedom:

$$n = 3(M - 1) - 2c_1 - c_2 \qquad (1)$$

Where M is the number of members including the frame, and c_k is the number of pairs of class k, which allows k degrees of freedom, preventing $3 - k$ (with $k = 1,2$) degrees each.

In the cases at hand, we have kinematic couplings with $k = 1$: each of the four rotary pairs prevents the two relative translations between the connecting rods.

4.2 Kinematic Analysis

Applying Grubler's equation to the articulated quadrilateral for $M = 4$, we get a single degree of freedom, thus a single free coordinate:

$$n = 3(4 - 1) - 2 \cdot 4 = 1 \qquad (2)$$

The closure equations of the quadrilateral are then the starting point for the following analysis:

$$\begin{cases} DA\ cos(\theta_{DA}) + AB\ cos(\theta_{AB}) + BC\ cos(\theta_{BC}) + CD\ cos(\theta_{CD} + \pi) = 0 \\ DA\ sin(\theta_{DA}) + AB\ sin(\theta_{AB}) + BC\ sin(\theta_{BC}) + CD\ sin(\theta_{CD} + \pi) = 0 \end{cases} \quad (3)$$

The angle θ_{AB} covered by the input link *AB* attached to the motor has been chosen as the free coordinate.

Now, since all rod dimensions are constant and θ_{DA} is fixed, as it is the angle between the two frame connections, the only unknowns are θ_{BC} and θ_{CD}, both functions of θ_{AB}. To find the unknowns in this nonlinear arrangement, the Newton-Raphson method can be implemented, starting from a suitable initial solution θ_{BC*} and θ_{CD*} and following the algorithm:

$$sol_{i+1} = sol_i - J_i^{-1} f_i \quad (4)$$

Where the closure equation f_i, the Jacobian Matrix J_i, and the solution sol_i calculated for each iteration i are presented in the following formulas:

$$f_i = \begin{bmatrix} DA\ cos(\theta_{DAi}) + AB\ cos(\theta_{ABi}) + BC\ cos(\theta_{BCi}) + CD\ cos(\theta_{CDi} + \pi) \\ DA\ sin(\theta_{DAi}) + AB\ sin(\theta_{ABi}) + BC\ sin(\theta_{BCi}) + CD\ sin(\theta_{CDi} + \pi) \end{bmatrix} \quad (5)$$

$$J_i = \begin{bmatrix} -BC\ sin(\theta_{BCi}) & -CD\ sin(\theta_{CDi} + \pi) \\ BC\ cos(\theta_{BCi}) & CD\ cos(\theta_{CDi} + \pi) \end{bmatrix} \quad (6)$$

$$sol_i = \begin{bmatrix} \theta_{BCi} \\ \theta_{CDi} \end{bmatrix} \quad (7)$$

4.2.1 Position Analysis

Knowing all the angles, the calculation of the position vectors of the three moving links *AB, BC, CD* follows directly:

$$\boldsymbol{r}_{AB} = AB\begin{bmatrix} cos(\theta_{AB}) \\ sin(\theta_{AB}) \\ 0 \end{bmatrix}, \qquad \boldsymbol{r}_{BC} = BC\begin{bmatrix} cos(\theta_{BC}) \\ sin(\theta_{BC}) \\ 0 \end{bmatrix}, \qquad \boldsymbol{r}_{CD} = CD\begin{bmatrix} cos(\theta_{CD}) \\ sin(\theta_{CD}) \\ 0 \end{bmatrix} \tag{8}$$

Finally, the position of the tip T of the claw can be obtained starting from point C, extending of T_1 from the line of BC and by T_2 in a direction orthogonal to T_1 (rotating counterclockwise).

4.2.2 Velocity Analysis

From the position vectors and the angular velocity ω_{AB}, the velocity of point B can be found as follows:

$$\boldsymbol{v}_B = \omega_{AB} \times \boldsymbol{r}_{AB} \tag{9}$$

Velocity at C can be calculated in two different ways:

$$\boldsymbol{v}_{C1} = \boldsymbol{v}_B + \omega_{BC} \times \boldsymbol{r}_{BC} \tag{10}$$

$$\boldsymbol{v}_{C2} = \omega_{CD} \times \boldsymbol{r}_{CD} \tag{11}$$

Equating the two velocities $\boldsymbol{v}_{C1} = \boldsymbol{v}_{C2}$ and solving for ω_{BC} and$d$ ω_{CD} it is possible to find the two angular velocities and the value of $\boldsymbol{v}_C$.

4.2.3 Acceleration Analysis

In the same way as in the velocity analysis, starting from the input angular acceleration, α_{AB}, it is possible to find the acceleration of B:

$$\boldsymbol{a}_B = \alpha_{AB} \times \boldsymbol{r}_{AB} - (\omega_{AB})^2 \boldsymbol{r}_{AB} \tag{12}$$

And the acceleration of C:

$$\boldsymbol{a}_{C1} = \boldsymbol{a}_B + \alpha_{BC} \times \boldsymbol{r}_{BC} - (\omega_{BC})^2 \boldsymbol{r}_{BC} \tag{13}$$

$$\boldsymbol{a}_{C2} = \alpha_{CD} \times \boldsymbol{r}_{CD} - (\omega_{CD})^2 \boldsymbol{r}_{CD} \quad (14)$$

$$\boldsymbol{a}_{C1} = \boldsymbol{a}_{C2} \quad (15)$$

For the purposes of the dynamic analysis, also the accelerations of the three moving bars centres of mass of *AB*, *BCT*, *CD* have been calculated:

$$\boldsymbol{a}_{B} = \frac{\alpha_{AB} \times \boldsymbol{r}_{AB} - (\omega_{AB})^2 \boldsymbol{r}_{AB}}{2} \quad (16)$$

$$\boldsymbol{a}_{BCT} = \boldsymbol{a}_{B} + \alpha_{BC} \times \boldsymbol{d}_{BG} - (\omega_{BC})^2 \boldsymbol{d}_{BG} \quad (17)$$

$$\boldsymbol{a}_{CD} = \frac{\alpha_{CD} \times \boldsymbol{r}_{CD} - (\omega_{CD})^2 \boldsymbol{r}_{CD}}{2} \quad (18)$$

Where $\boldsymbol{d}_{BG} = \begin{bmatrix} \frac{BC+T_1}{2} \\ \frac{T_2}{2} \\ 0 \end{bmatrix}$ is the vector from B to the centre of mass of the claw.

A MATLAB script was then developed to perform the complete kinematic analysis for each input of θ_{AB}. Notably, already with the position analysis and considering a constant rotational velocity of *AB*, a good estimate of the mechanism behaviour could be extrapolated for example by plotting the trajectory of the tip of the claw *T* in the plane at regular angles θ_{AB}. This provides a visual representation where denser parts represent lower velocity of the tip and could also give a clear sight on the range of motion of the moving bars. As an example,

Figure 11 shows a four-bar linkage configuration in which the claw tip decelerates until inverting the motion along the x axis. The denser part at the end of the trajectory circled in red on the left graph corresponds to the highlighted part of the right graph. Although, performing a complete kinematics analysis allows for a better understanding of the general mechanism's behaviours under specific conditions and could be reused for further studies, such as in simulating the motor actuation through a specific profile of acceleration.

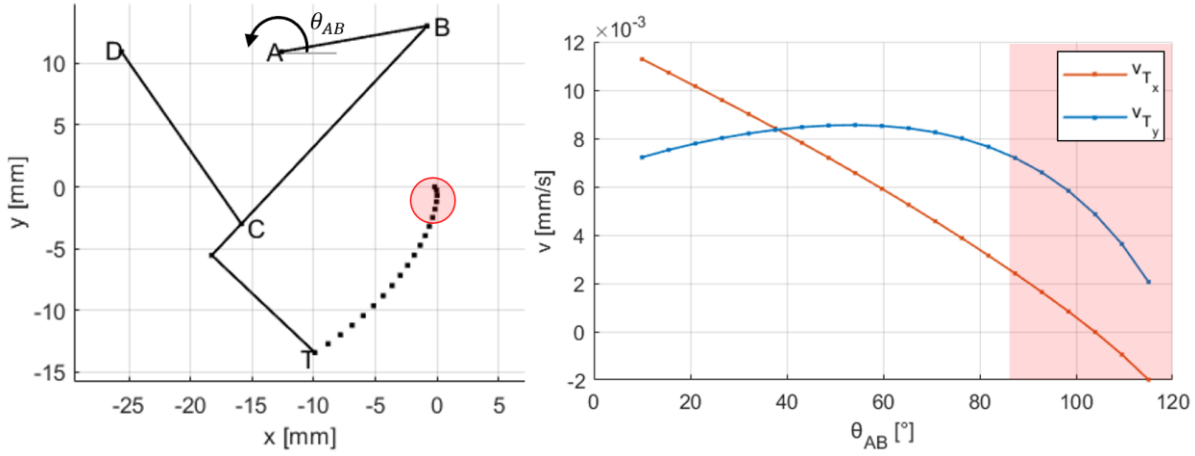

Figure 11: example of four-bar configuration. On the left side is presented the tip trajectory, while on the right side the velocities along x and y.

4.3 Force Analysis

Knowing the position of the claw tip T from the kinematic analysis and the torque T_A delivered by the stepper motor from the component selection, the force analysis has been applied to evaluate the amount of force transferred from the actuation of the claw to the drogue. For the particular solution of this problem, some simplifications could be introduced: to evaluate the force at the claw tip, the vector $\boldsymbol{r}_{AT}$ between the motor centre A and the point T can be used as the lever arm to directly calculate the actual force with an expected good approximation.

$$\boldsymbol{F}_T = \frac{T_A \times \boldsymbol{r}_{AT}}{\boldsymbol{r}_{AT} \cdot \boldsymbol{r}_{AT}} \qquad (19)$$

For a more complete dynamic analysis, forces and torques are computed for each three of the moving links AB, BCT and CD, with the momentum of inertia I_{AB}, I_{BCT}, I_{CD} and masses m_{AB}, m_{BCT}, m_{CD} calculated through SolidWorks.

Starting with AB, the momentum equilibrium has been calculated from the centre of gravity, which is located at $\frac{AB}{2}$ from A, so the three equilibrium equations are:

$$F_{Ax} - F_{Bx} = m_{AB}\, a_{ABx} \qquad (20)$$

$$F_{Ay} - F_{By} = m_{AB}a_{ABy} \quad (21)$$

$$T_A + F_{Ax}\frac{AB}{2}sin(\theta_{AB}) - F_{Ay}\frac{AB}{2}cos(\theta_{AB}) + F_{Bx}\frac{AB}{2}sin(\theta_{AB}) + \\ - F_{By}\frac{AB}{2}cos(\theta_{AB}) = I_{AB}\alpha_{AB} \quad (22)$$

The body *BCT* has its centre of gravity *G* located at distance d_{BG} from *B*, which is chosen as the pole for the momentum equilibrium, and distance d_{CG} from C and d_{TG} from T.

$$d_{BG} = \sqrt{\left(\frac{BC + T_1}{2}\right)^2 + \left(\frac{T_2}{2}\right)^2} \quad (23)$$

$$d_{CG} = \sqrt{\left(\frac{BC + T_1}{2} - BC\right)^2 + \left(\frac{T_2}{2}\right)^2} \quad (24)$$

$$d_{TG} = \sqrt{\left(-\frac{BC + T_1}{2}\right)^2 + \left(-\frac{T_2}{2}\right)^2} \quad (25)$$

The three equilibrium equations are then:

$$F_{Bx} - F_{Cx} - F_T sin(\theta_{BC} + \theta_T) = m_{BCT}a_{BCx} \quad (26)$$

$$F_{By} - F_{Cy} + F_T cos(\theta_{BC} + \theta_T) = m_{BCT}a_{BCy} \quad (27)$$

$$F_{Bx}d_{BG}sin(\theta_{BG} + \theta_{BC}) - F_{By}d_{BG}cos(\theta_{BG} + \theta_{BC}) + F_{Cx}d_{CG}sin(\theta_{CG} + \theta_{BC}) + \\ -F_{Cy}d_{CG}cos(\theta_{CG} + \theta_{BC}) + F_T cos(\theta_{TG} + \theta_{BC}) = I_{BC}\alpha_{BC} \quad (28)$$

For the last moving body, *CD*, the momentum equilibrium pole has been chosen in the centre of gravity which lays at $\frac{CD}{2}$ from *C* and final three equations of equilibrium are:

$$F_{Cx} - F_{Dx} = m_{CD}a_{CDx} \quad (29)$$

$$F_{Cy} - F_{Dy} = m_{CD}a_{CDy} \quad (30)$$

$$F_{Cx}\frac{CD}{2}sin(\theta_{CD}) - F_{Cy}\frac{CD}{2}cos(\theta_{CD}) + F_{Dx}\frac{CD}{2}sin(\theta_{CD}) + \\ -F_{Dy}\frac{CD}{2}cos(\theta_{CD}) = I_{CD}\alpha_{CD} \tag{31}$$

There are 9 unknowns: $F_{Ax}, F_{Bx}, F_{Cx}, F_{Dx}, F_{Ay}, F_{By}, F_{Cy}, F_{Dy}, F_T$, so the system is solvable.

Implementing it as a matrix system as in *eq. 32*, the solutions can be evaluated easily in a MATLAB script, with particular regard to the force F_T, which is the one that ultimately keeps the drogue locked in case of external solicitations:

$$\begin{bmatrix} 1 & 0 & -1 & 0 & 0 & 0 & 0 & 0 & 0 \\ 0 & 1 & 0 & -1 & 0 & 0 & 0 & 0 & 0 \\ \frac{AB}{2}s\theta_{AB} & -\frac{AB}{2}c\theta_{AB} & \frac{AB}{2}s\theta_{AB} & -\frac{AB}{2}c\theta_{AB} & 0 & 0 & 0 & 0 & 0 \\ 0 & 0 & 1 & 0 & -1 & 0 & 0 & 0 & s(\theta_{BC}+\theta_T) \\ 0 & 0 & 0 & 1 & 0 & -1 & 0 & 0 & c(\theta_{BC}+\theta_T) \\ 0 & 0 & d_{BG}s(\theta_{BG}+\theta_{BC}) & -d_{BG}c(\theta_{BG}+\theta_{BC}) & d_{CG}s(\theta_{CG}+\theta_{BC}) & -d_{CG}c(\theta_{CG}+\theta_{BC}) & 0 & 0 & c(\theta_{TG}+\theta_{BC}) \\ 0 & 0 & 0 & 0 & 1 & 0 & -1 & 0 & 0 \\ 0 & 0 & 0 & 0 & 0 & 1 & 0 & -1 & 0 \\ 0 & 0 & 0 & 0 & -\frac{CD}{2}s\theta_{CD} & -\frac{CD}{2}c\theta_{CD} & \frac{CD}{2}s\theta_{CD} & -\frac{CD}{2}c\theta_{CD} & 0 \end{bmatrix} \begin{bmatrix} F_{A_x} \\ F_{A_y} \\ F_{B_x} \\ F_{B_y} \\ F_{C_x} \\ F_{C_y} \\ F_{D_x} \\ F_{D_y} \\ F_T \end{bmatrix} = \begin{bmatrix} m_{AB}\, a_{ABx} \\ m_{AB}a_{ABy} \\ I_{AB}\alpha_{AB} \\ m_{BCT}a_{BCx} \\ m_{BCT}a_{BCy} \\ I_{BC}\alpha_{BC} \\ m_{CD}a_{CDx} \\ m_{CD}a_{CDy} \\ I_{CD}\alpha_{CD} \end{bmatrix} \tag{33}$$

5. Comprehensive System Understanding and Configuration Evolution

5.1 Kinematic Analysis of the Original Design

Based on the position analysis explained in *Chapter 4.2.1*, the path of the original claw can be visualized in *Figure 12*, where the axis origin has been centred in the point of contact between the drogue and the claw tip, giving insights on the total horizontal and vertical length of the path.

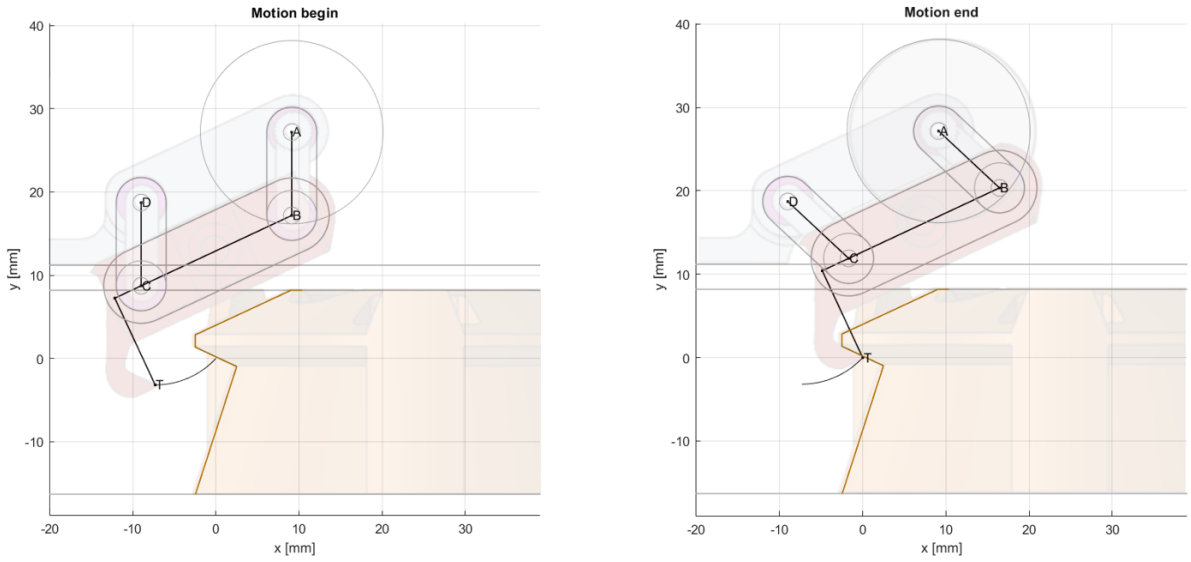

Figure 12: original claw tip movement.

The original mechanism consists of a parallelogram, with the length of the four bars reported in *Table 2*. With this configuration, the input link *AB* rotates from -90° to -43° and shares the same angular rotation of the output link *CD*, which describes the same motion. As a consequence, the claw moves along its path without rotating, making the locking movement a perfect translation.

Element	AB	BC	CD	DA	T_1	T_2
Length (mm)	10	20	10	20	4.3	12.2

Table 2: original linkage lengths

The MATLAB kinematic and force analysis proposed in *Chapter 4* were subsequently cross-referenced with the Working Model simulation to ensure comparability in both motion and forces. For both the Working model and MATLAB simulations firstly a constant speed of the motor was set, to evaluate the kinematic analysis model and then a torque of 20mNm was considered applied to the joint *A* corresponding to the motor shaft while the mechanism was on its final position, fully closed around the drogue to analyse the force. The velocities of the tip along the curve, and force of contact between the claw and the drogue at the end of the motion are presented respectively in *Figure 13* and i*n Table 3*.

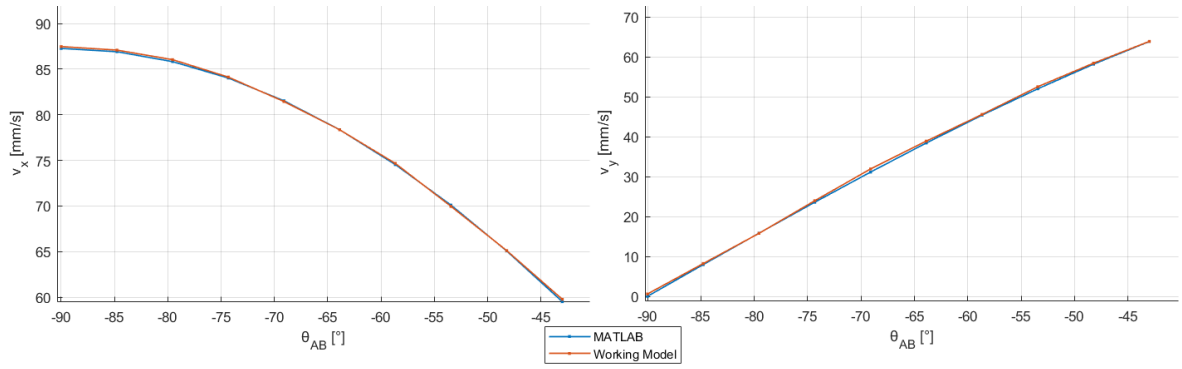

Figure 13: velocities of the claw tip in MATLAB and Working Model.

	Working Model	MATLAB
$\lvert \boldsymbol{F}_T \rvert$	2.07N	0.35N
$\theta_{\boldsymbol{F}_T}$	64.9°	-18.5°

Table 3: force of contact with simplification

Observing *Figure 13,* the results of the kinematic analysis introduced in *Chapter 4.2* are consistent with the measurements obtained from the Working Model simulation. On the contrary, the simplifications introduced in *Chapter 4.3* considering the force $\boldsymbol{F}_T$ as $\boldsymbol{T}_A = \boldsymbol{r}_{AT} \times \boldsymbol{F}_T$ have proven to be incorrect and *Table 3* presents discrepancies compared with the values of the simulation. Specifically, after a deeper analysis, for positions of the claw tip to the left of the vertical from point *A*, as illustrated in *Figure 14*, the computed force exhibited a negative vertical component, even though the claw trajectory was in the upward phase. In addition, the simplification introduced a crucial oversight by neglecting the actual shape of the two components in contact. While the claw tip could be reasonably assumed to be point-like, the surface of the drogue in contact with the claw tip has a precise angle and the resulting contact force must be perpendicular to this angle, a consideration overlooked by the introduced simplification.

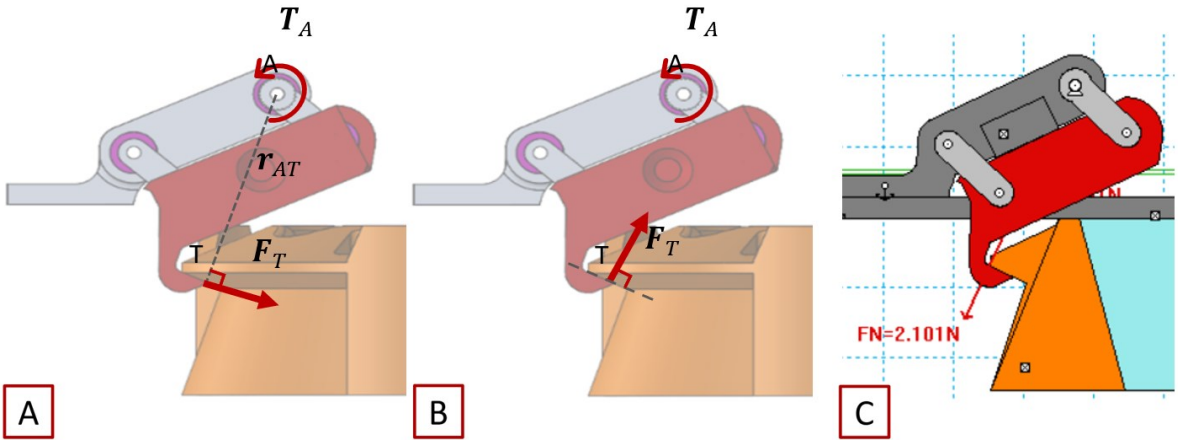

Figure 14: comparison between simplification (A), expected behaviour (B) and simulation (C)

Therefore, from that moment the more complete force analysis has been considered and the results for the starting configuration are reported in *Table 4*. The force at closure, calculated with the dynamic analysis, for a torque of 20mNm

reached a value of 0.89N along *x* and 1.90N along *y*, oriented at 65° from the horizontal, returning similar values to the ones of the Working Model simulation.

	Working Model	MATLAB
$\lvert \boldsymbol{F}_T \rvert$	2.11N	2.10N
$\theta_{\boldsymbol{F}_T}$	64.9°	65°
$\boldsymbol{F}_A = -\boldsymbol{F}_B$	2.04N	1.98N
$\boldsymbol{F}_C = -\boldsymbol{F}_D$	0.89N	0.70N

Table 4: Complete force analysis comparison

5.2 Extra Rotation

After understanding the range of operability of the mathematical model, the first parameter to be defined with the objective of improving the locking capabilities of the mechanism was the extent of extra rotation of link *AB* in respect to the vertical axes, to hold the locked position. In this stage an angle of 25° from the vertical was considered enough to avoid motor missteps and to be effective against external forces on the claw tip. However, changing only the starting and ending angles of the input *AB* to achieve the extra rotation without modifying the other links resulted in a impractical path, rendering the mechanism unusable: the total height of the path was comparable with the distance between the two spacecrafts, meaning an eventual interference during docking operations with misaligned satellites; the linkage collided with the drogue, while the motor compenetrated the satellite wall, as depicted in *Figure 15*. Also analysing the velocities in *Figure 16*, at the end of the motion the claw is inverting its motion ad is starting to open. Consequently, modifications were made in the next iterations to achieve a desirable path.

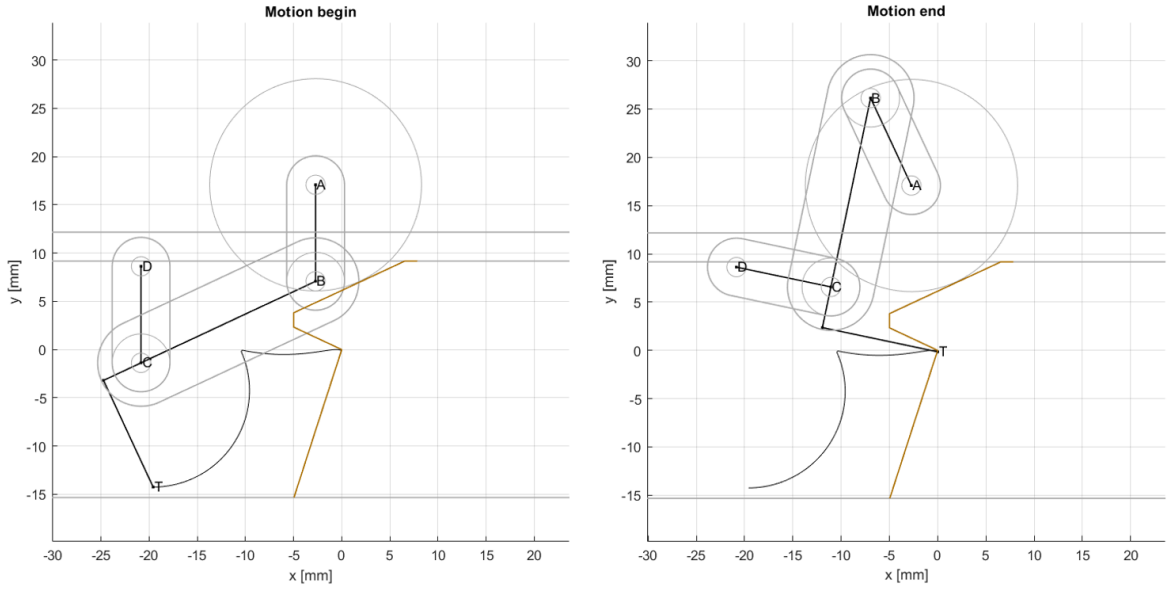

Figure 15: original linkage with extended path.

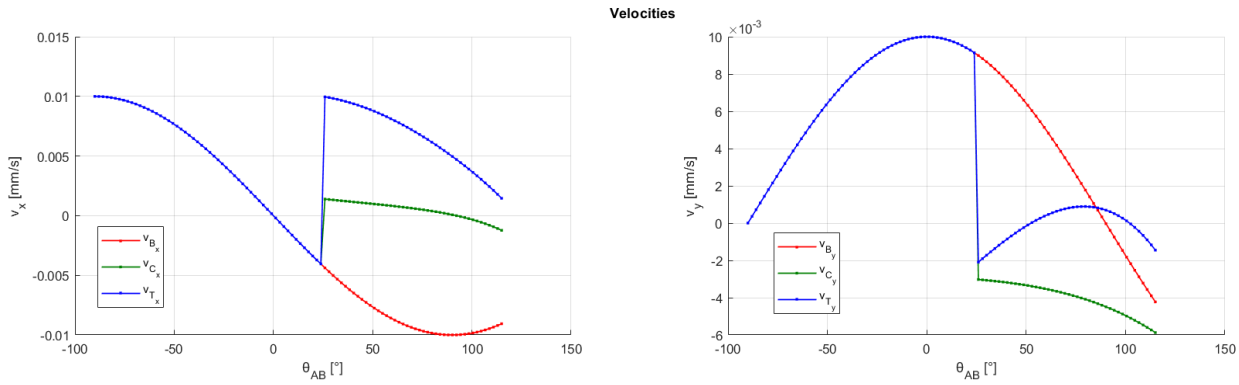

Figure 16: velocities of original linkage extended path.

5.3 First Batch of Iterations

Throughout this batch of iterations, the objective is to comprehend general behaviours of the mechanism as its components undergo modifications. Restoring spatial constraints for both the linkage and the motor, while simultaneously achieving a smoother coupler curve than the one discussed in *Chapter 5.2*, presented several challenges. As a synthesis of this stage of the design, three different configurations are presented here to describe some of the encountered critical aspects.

Configuration 1: the original one, with the change of *CD* and T_1, T_2 accordingly to keep a proper distance from the plate to place the motor.

Element	AB	BC	CD	DA	T_1	T_2
Length (mm)	10	20	18.75	20	15.5	1.5

Table 5: configuration 1.

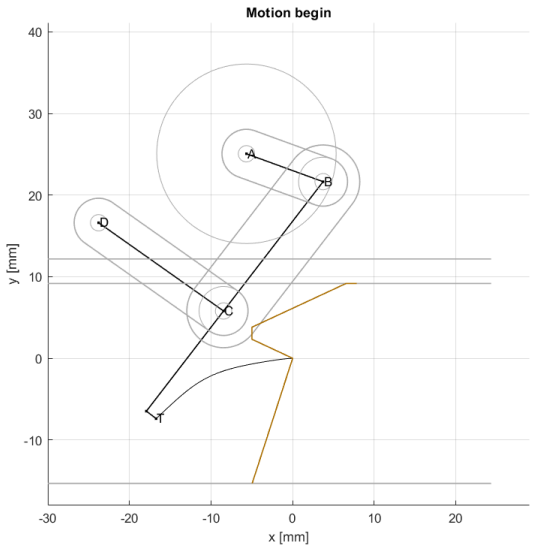

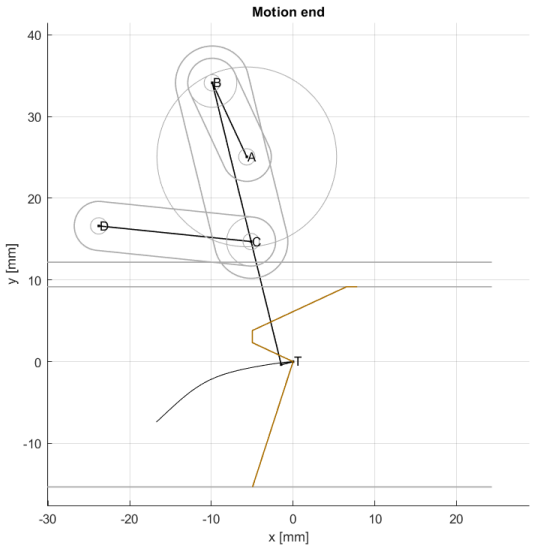

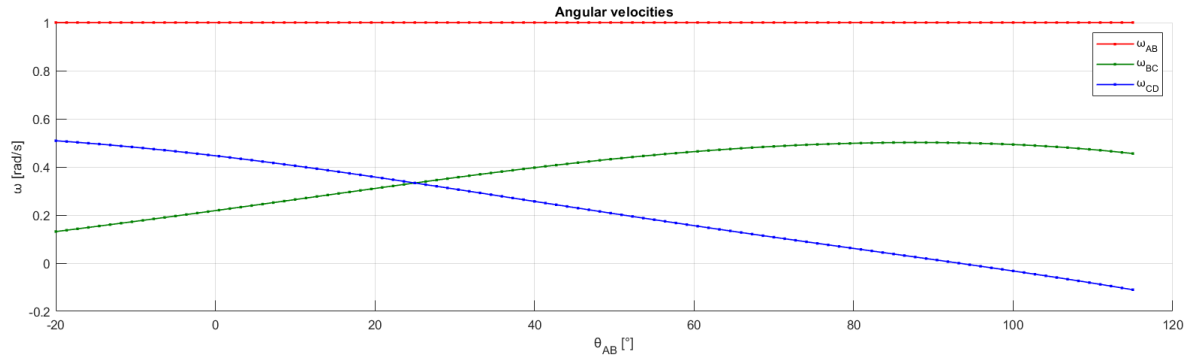
Angular velocities
ω [rad/s]
θ_AB [°]
ω_AB
ω_BC
ω_CD

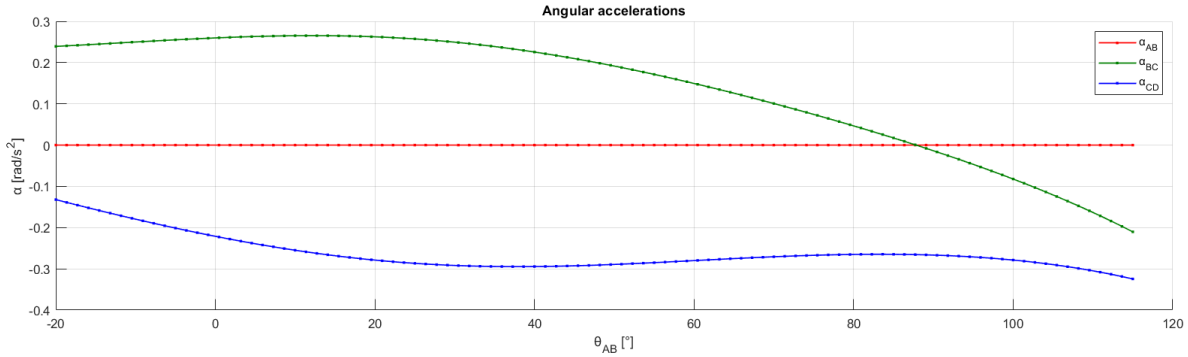
Angular accelerations
α [rad/s²]
θ_AB [°]
α_AB
α_BC
α_CD

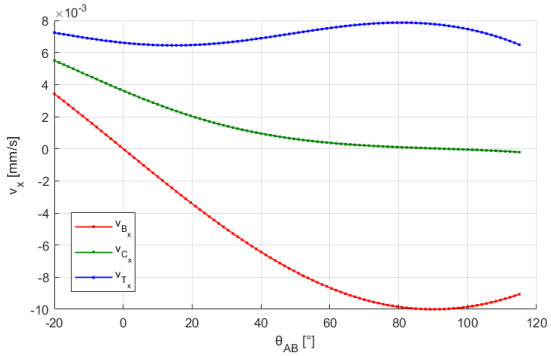
×10⁻³
v_x [mm/s]
θ_AB [°]
v_B_x
v_C_x
v_T_x

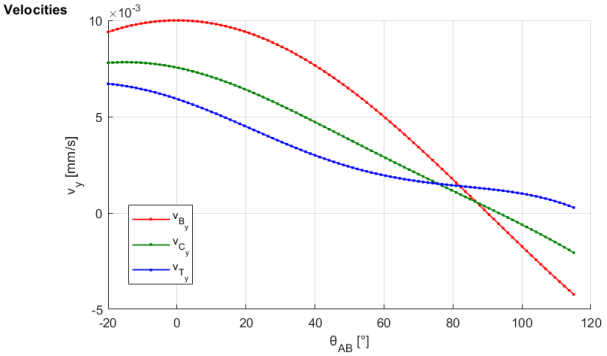
Velocities
×10⁻³
v_y [mm/s]
θ_AB [°]
v_B_y
v_C_y
v_T_y

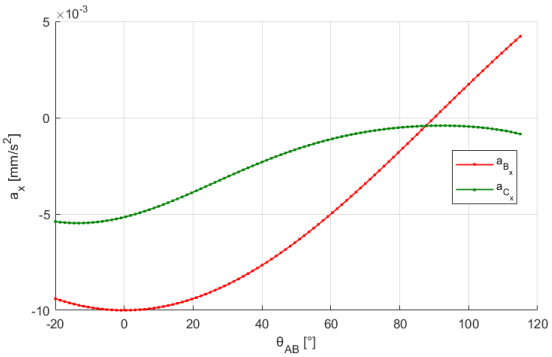
×10⁻³
a_x [mm/s²]
θ_AB [°]
a_B_x
a_C_x

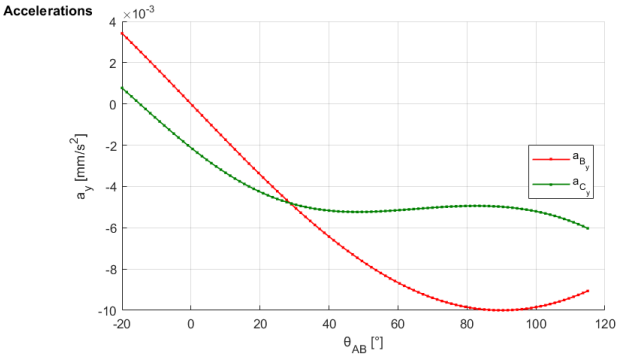
Accelerations
×10⁻³
a_y [mm/s²]
θ_AB [°]
a_B_y
a_C_y

Configuration 2: maintains the same parameters of Configuration 1, except for the frame angle θ_{DA}, which has been changed to 10° instead of 25°.

Element	AB	BC	CD	DA	T_1	T_2
Length (mm)	10	20	18.75	20	15.5	1.5

Table 6: configuration 2.

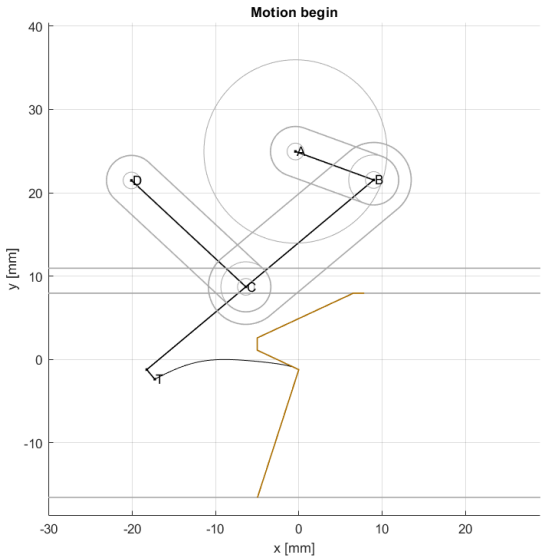

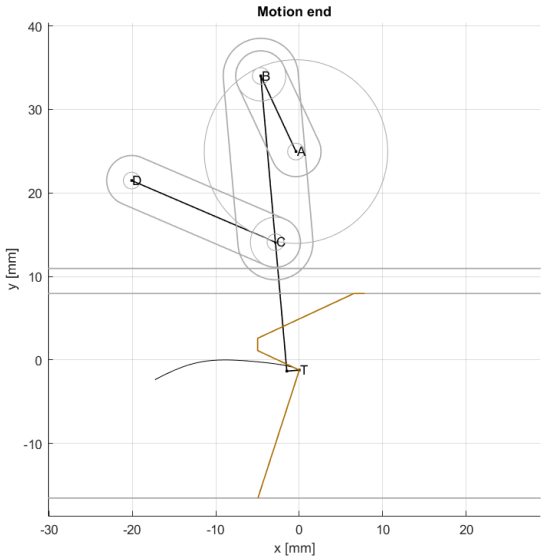

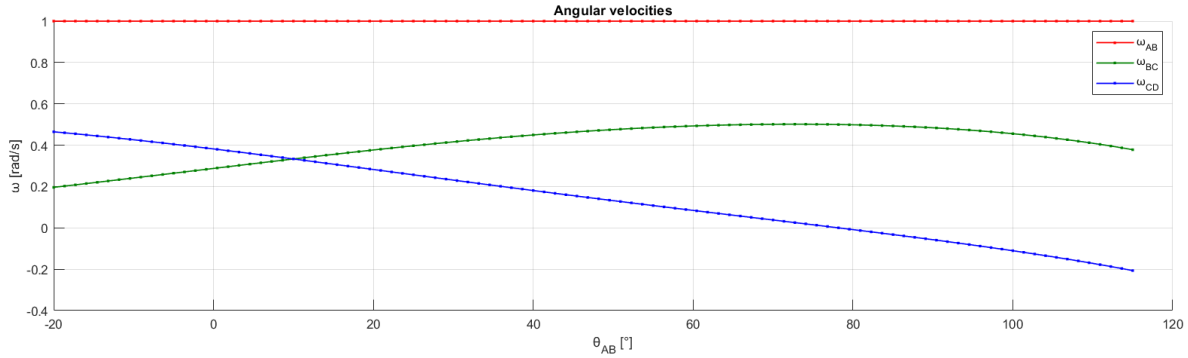
Angular velocities
ω [rad/s]
θAB [°]
ωAB
ωBC
ωCD

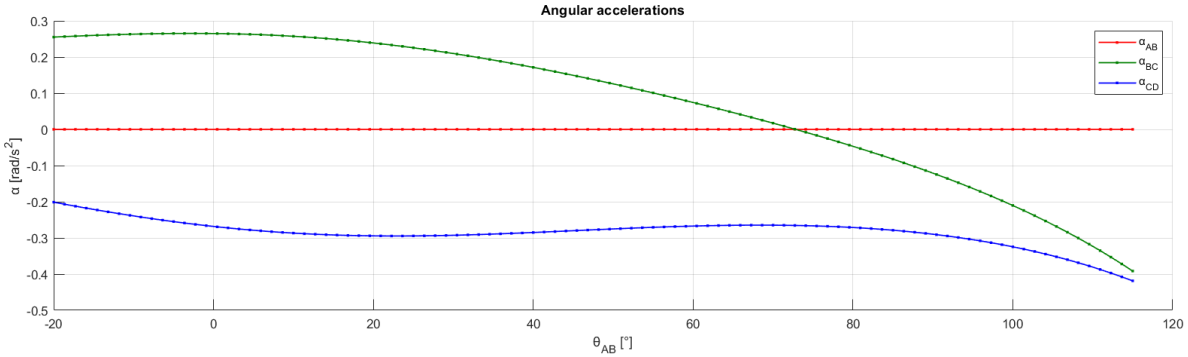
Angular accelerations
α [rad/s2]
θAB [°]
αAB
αBC
αCD

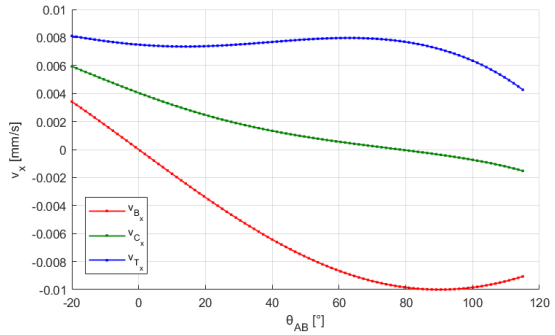
vx [mm/s]
θAB [°]
vBx
vCx
vTx

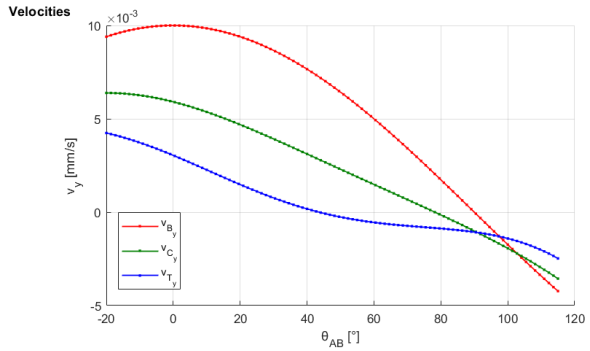
Velocities
×10-3
vy [mm/s]
θAB [°]
vBy
vCy
vTy

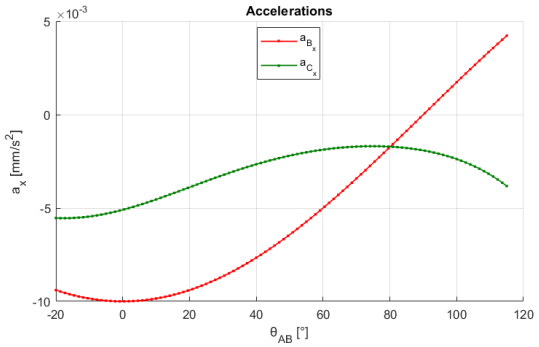
Accelerations
×10-3
ax [mm/s2]
θAB [°]
aBx
aCx

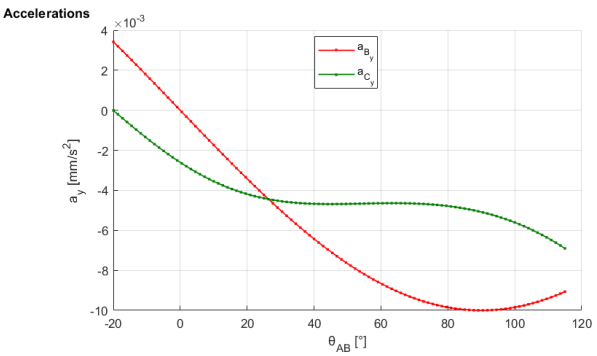
Accelerations
×10-3
ay [mm/s2]
θAB [°]
aBy
aCy

Configuration 3: changing all the linkage lengths, while maintaining the same frame angle θ_{DA} of the original configuration.

Element	AB	BC	CD	DA	T_1	T_2
Length (mm)	8	24.5	14	16	11	6.5

Table 7: configuration 3.

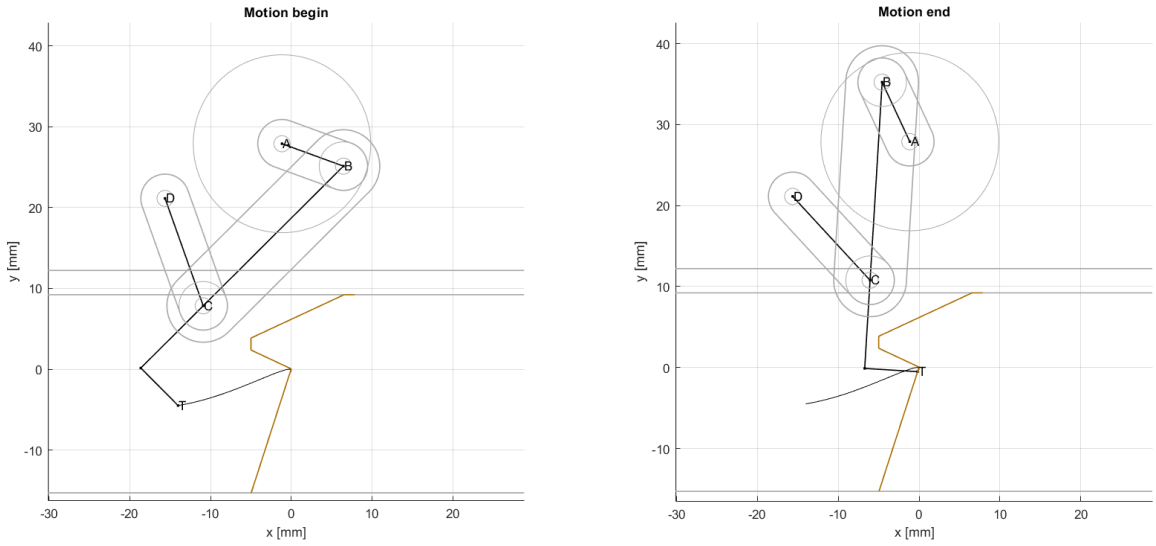

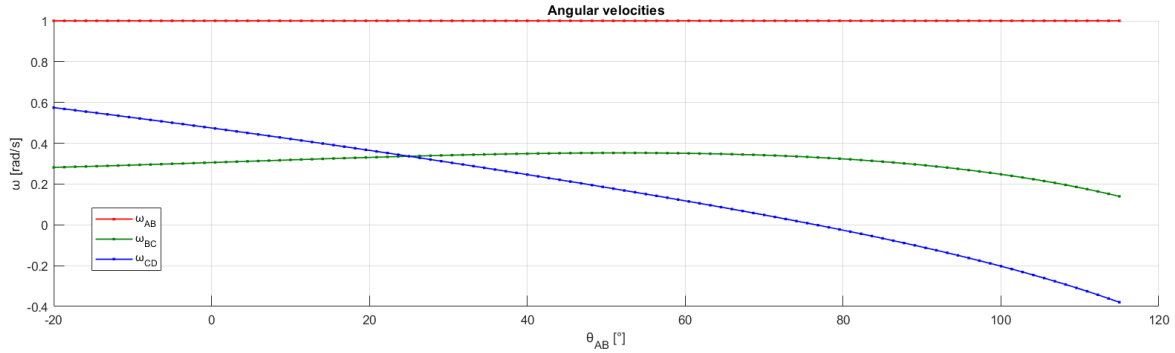
Angular velocities
ω [rad/s]
θ_AB [°]
ω_AB
ω_BC
ω_CD

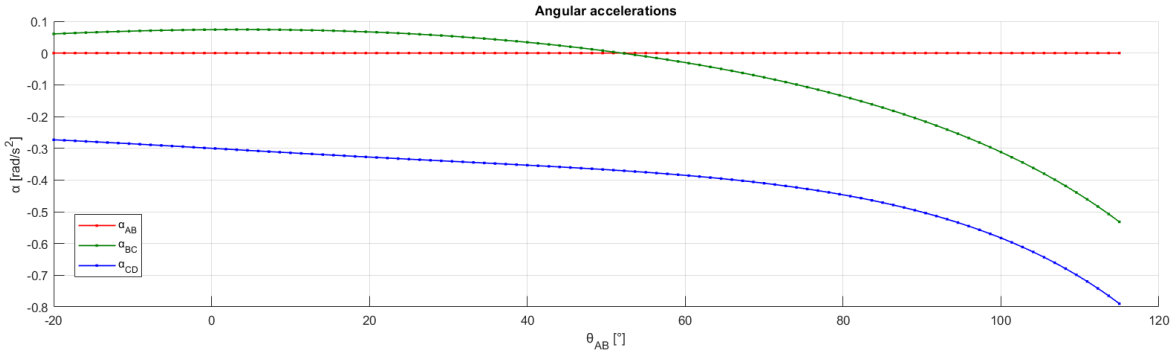
Angular accelerations
α [rad/s^2]
θ_AB [°]
α_AB
α_BC
α_CD

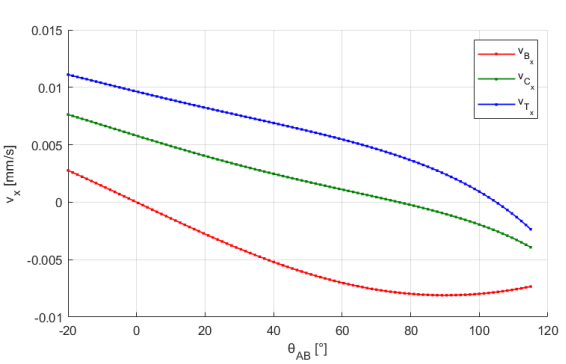
v_x [mm/s]
θ_AB [°]
v_Bx
v_Cx
v_Tx

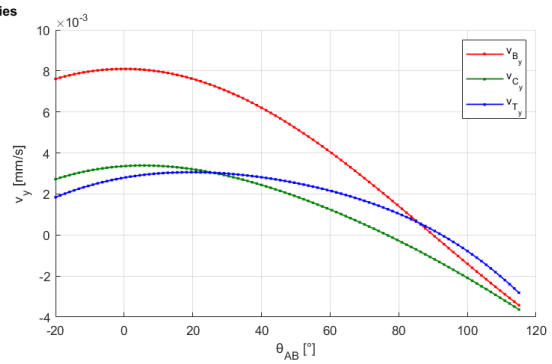
Velocities
v_y [mm/s]
θ_AB [°]
v_By
v_Cy
v_Ty

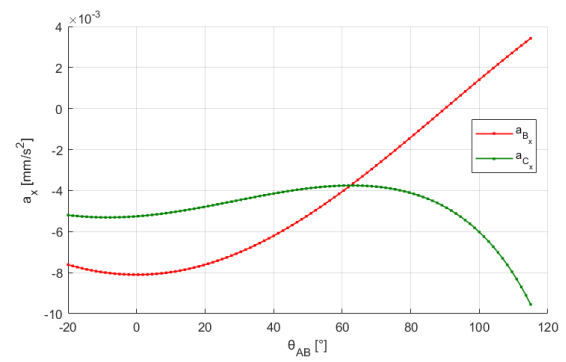
Accelerations
a_x [mm/s^2]
θ_AB [°]
a_Bx
a_Cx

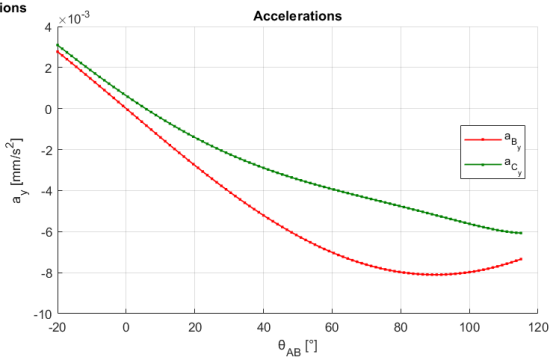
Accelerations
a_y [mm/s^2]
θ_AB [°]
a_By
a_Cy

In the exploration of different configurations for the system, the coupler curve manifested different behaviours.

In *Configuration 1* the modifications in the lengths of *CD* and T_1, T_2 aim to restore the spatial constrains for both the linkage and the motor while obtaining a smoother coupler curve. After the modifications, the curve results smoother, but the tip trajectory still retains a notable vertical profile, impacting the overall system dynamics. This shows that isolated adjustments to individual components in the four-bar linkage may have unintended consequences on the overall motion.

In *Configuration 2* instead of changing the lengths of components, only the frame angle θ_{DA} was modified, to observe the effects of rotating the whole 4-bar linkage in achieving a predominantly horizontal path. This configuration demonstrates success in maintaining a nearly flat trajectory for a substantial portion. However, as the system progresses to $\theta_{AB} = 43°$, the coupler curve reaches its maximum height -or minimum distance from the chaser's wall- and subsequently, an inversion in the vertical trend occurs, resulting in an ineffective closure as reported in *Figure 17*.

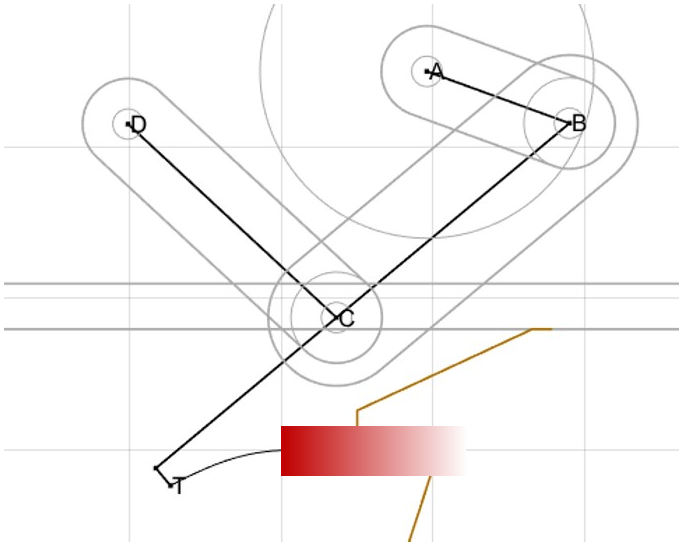

Figure 17: detail of Configuration 2. In red the decreasing part of the trajectory.

In *Configuration 3* a complete resize of all four components is made to achieve a quasi-horizontal path throughout the motion and, while successful in maintaining a predominantly horizontal trajectory, the coupler curve in *Configuration 3* still presents an inversion of motion for the claw at the end of the trajectory, leading to an incomplete blockage as showed in *Figure 18*.

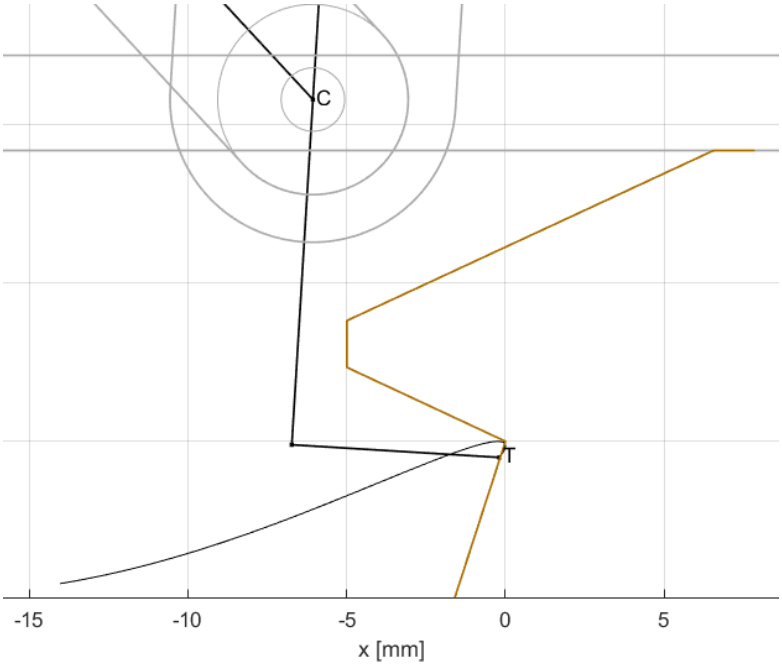

Figure 18: zoom on Configuration 3 with inversion of motion at closure.

Despite the overall attempts to improve the claw trajectory, these three configurations highlights the complexity of achieving a seamless closure and presents some hints to take care of in the next iterations, such as the effect of rotation of the frame link *DA* and the frequent presence of the vertical maximum before the end of the trajectory leading to a loose closure that will be further discussed in the next sections.

5.3.1 Gap at Closure

Because B reaches its maximum height at $\theta_{AB} = 90°$ with respect to the horizontal, it was suspected that as a general consequence the new configuration had the claw tip to behave similarly, reaching the minimum distance from the plate before completing its motion and leaving a gap with the drogue that had to be compensated. After computing some iterations in the design and analysing the claw path, most of the curves presented a minimum distance between the point T and the x axis before the complete rotation. For this reason, a first hypothesis was to include an elastic element in the design to keep the drogue pushed against the claw at the minimum distance, compensating the gap at end of path.

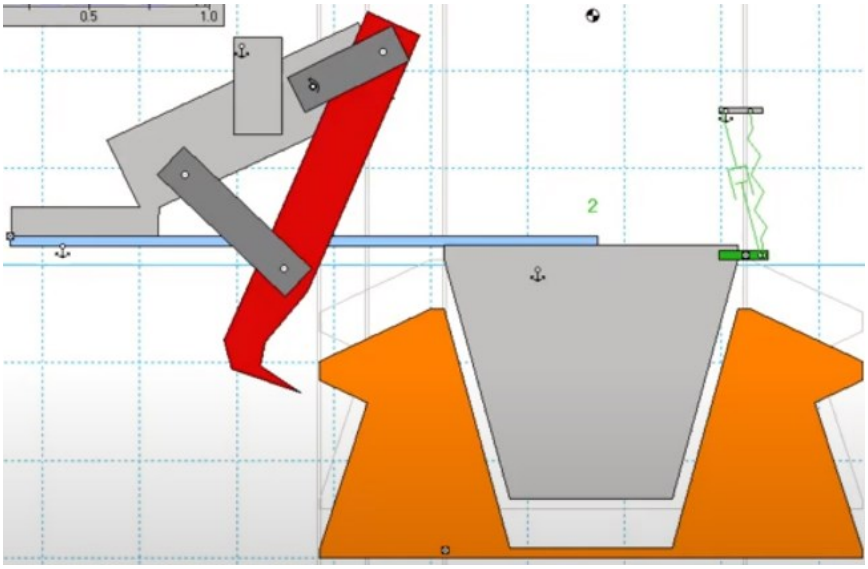

Figure 19: Working Model simulation with spring and dampener.

To size the elastic element to remain compressed, the force of contact between the claw tip and the drogue was calculated within the portion of the trajectory of the claw included in the Δy between the vertical peak and the height of the final position of the tip. Half of the minimum force obtained in this interval was set as the compressing one. An additional increment $\Delta y_2 = 0.5mm$ has then been added to keep the spring compressed after the end of motion. Considering the example in

Figure 20, with a Δy of 0.3mm, the additional increment Δy_2 of 0.5mm and a compressing force of 1N, which is half of the actual one at claw tip, the required spring needs a k of 1.25N/mm, using the following equation:

$$k = \frac{\frac{F_{\min}}{2}}{\Delta y + \Delta y_2} \qquad (34)$$

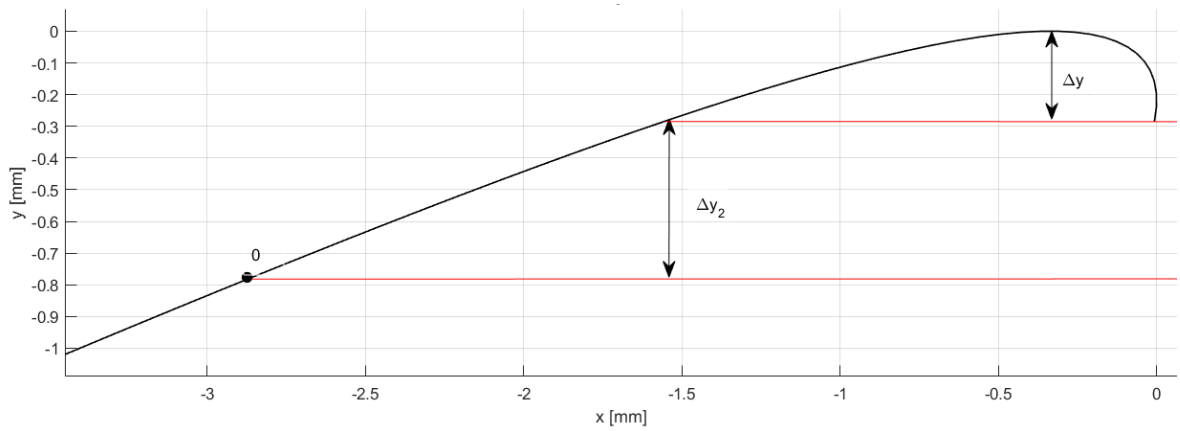

Figure 20: zoom on claw tip ending path.

The presence of this elastic element adds complexity in the whole system, especially during the real implementation, which implies an eventual modification of the drogue-probe shape or to find the proper location to place the new element without modifying other components. An alternative solution to completely avoid this addition has been explored in a second iteration of the design, focusing on configurations with the vertical peak of the coupler curve outside the range of motion of the mechanism or with a flatter portion in the nearby of the peak.

5.4 Second Batch of Linkage Iterations

During this phase, gaining deeper understanding on the system behaviour, some hints were obtained in the process and can be reported as follows.

5.4.1 Frame link rotations

First of all, in the context of four-bar mechanisms, each configuration presents a unique coupler curve and when the frame link undergoes rotation, the shape of the coupler curve remains constant, simply rotating along with the linkage. Considering the imposition of specific initial and final angles θ_{AB} for the input link with respect to the horizontal axis, this effectively selects a distinct segment of the coupler link. When the frame link is rotated –concurrently rotating the entire linkage and, by extension, the coupler curve– both rotation and the selection of a different part of the coupler curve occurs. As an example, with initial and final angles $\theta_{AB_i} = 0°$ and $\theta_{AB_f} = 115°$, the selected portion of the coupler curve is highlighted in red in *Figure 21*. When the frame link is rotated about $\theta_{DA} = 10°$, the coupler curve rotates and the selected portion changes consequently, as highlighted in green in *Figure 21*. As a consequence of the rotation, and with consistent link lengths, increasing the inclination of the frame link *DA*, causes an overall increase in the curve's height Δy while decreasing the maximum horizontal extension Δx, for same initial and final θ_{AB} given that the coupler curve rotates along with it.

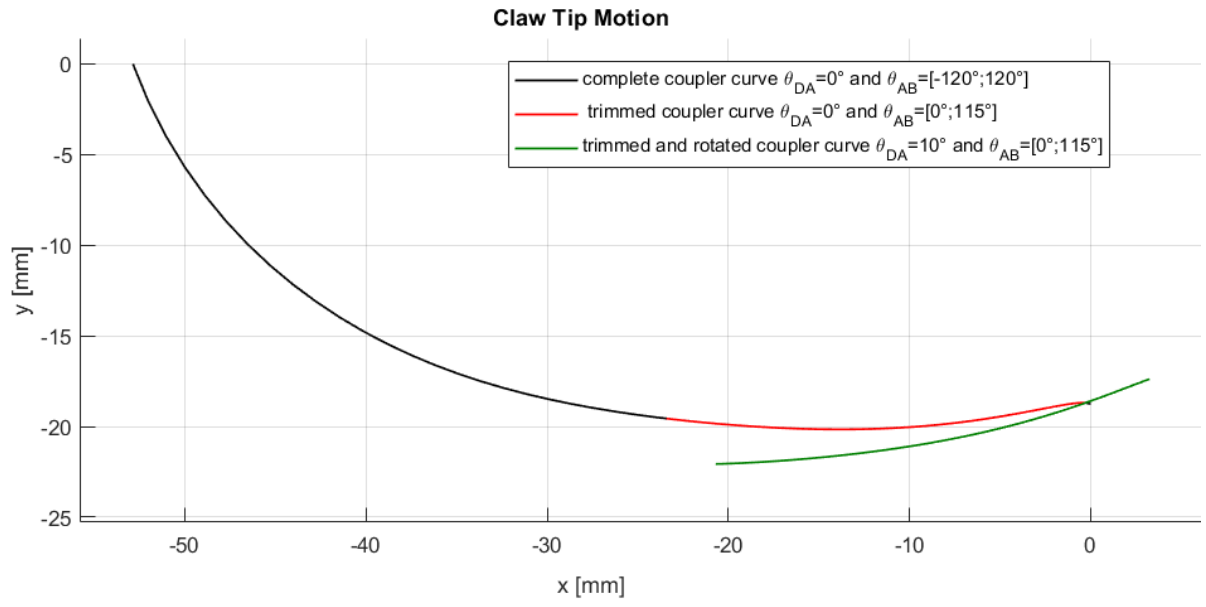

Figure 21: manipulation of coupler curve. Initial curve in black, selected portion before (in red) and after rotation (in green).

This behaviour becomes particularly useful when aiming to choose a flatter portion of the coupler curve while eliminating its inclination with respect to the horizontal and applying this insight in the context of this thesis implies that the rotation of the entire four-bar linkage can be harnessed beyond simply altering the orientation of the coupler curve, as explored in *Chapter 5.3* with *Configuration 2*. It can also have the potential of isolating specific parts of the coupler curve, allowing for the selection of the shape of the peak and of a flatter portion of the path.

5.4.2 Force increases at point of inversion

As a second hint, when the curve of the claw tip is tangent to the drogue surface, the torque force reaches a discontinuity and the tip reaches motion inversion. A solution with the final input link angle θ_{AB} too close to the inversion of motion of the claw can make the mechanism unreliable, having small tolerances in proximity of the inversion point (0.01mm) to cause rapid changes in the behaviour of the linkage, tending to open it if not properly constrained.

Designing the curve with the point of tangency for $\theta_{AB} = \theta_{AB_{end}} - 5°$ allows to exploit the initial inversion of the curve to avoid the opening taking place.

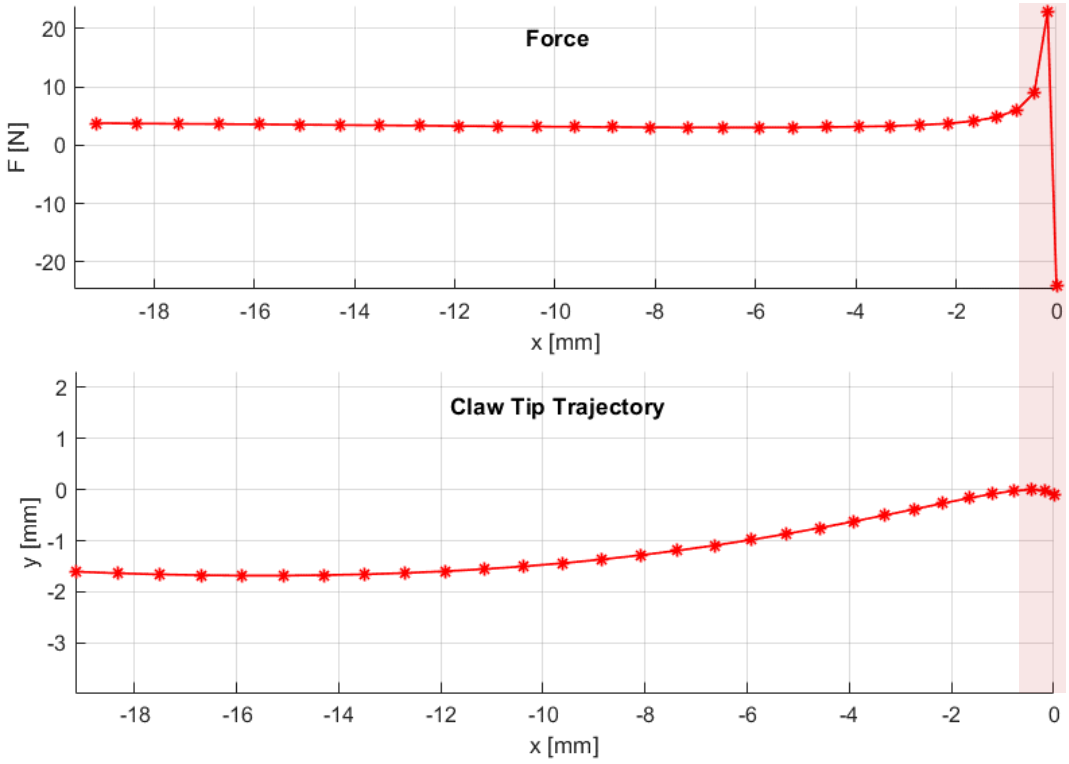

Figure 22: forces calculated at end of path. Highlighted area is in proximity of inversion.

In this phase, particular attention was dedicated in realizing a path that was horizontal, with a height between 1-5mm, to avoid excessive protruding of the claws in the opened position. To obtain the maximum force, the coupler curve has been crafted to move the vertical peak slightly before the end of the motion range, exploiting the minimal inversion. The formula for evaluating the force can be retrieved from the force analysis matrix in *eq. 35*:

$$F_T = \frac{T_A \cdot sin(\theta_{BC} - \theta_{CD})}{AB \cdot \left(sin(\theta_{AB} - \theta_{BC}) \cdot sin(\theta_{CD} + \theta_T) + \sqrt{\left(1 + \frac{T_1}{BC}\right)^2 + \left(\frac{T_2}{BC}\right)^2} \cdot sin(\theta_{AB} - \theta_{CD}) \cdot sin(\theta_{CT} - \theta_T) \right)}$$

(36)

5.5 Final Iterations and 3D Modelling

Considering the size of the actual components of the mechanism, some constraints were then made on the length of the four links, obtaining the final lengths reported in *Table 8*.

Element	**AB**	**BC**	**CD**	**DA**	T_1	T_2
Length (mm)	12	22	17	13	15.7	2

Table 8: final links

In the final stages of the design process, the real components were implemented through SolidWorks modelling, and a trade-off between optimal force and compactness was reached. In these last iterations, the challenges related to trajectory observed in previous chapters were successfully addressed, obtaining a functional design that aligns with expectations and requirements. Further details on the obtained performance will be discussed in the *Chapter 7*, while accounting for the physical dimensions of the components, some constraints were imposed on the sizes of the four links, resulting in the final lengths in *Table 8*. More in detail, the claw needed to accommodate the two ball bearing joints, so a width of 9mm was set as the minimum and for the same reason the length of *BC* could not be less than 9mm, while to give enough available surface of contact with the drogue, the thickness was set to 10mm. The shape of the claw has been modelled to match with the surface of the drogue. For the input and output links, *AB* and *CD*, the minimum width was set to 5mm, hosting only 2mm pins, but has been raised to 6mm to give additional strength, while the thickness was set to 3mm. For the two lengths, the minimum was considered as the 10mm of the original design. The link *AD* has been designed in accordance with the size and position of the other components on the plate. More specifically, point A coincides with the motor shaft, held in place at the correct distance from the plate by a modelled housing component, meanwhile

point D is located at the centre of the ball bearing housing in the other frame element in *Figure 23*.

To complete the functional setup and obtain passive closure at the end of motion, an additional piece has then been modelled to abut the mechanism. To avoid excessive loads on the link AB, it was decided to abut the claw BCT instead, which is thicker. As a mean of detection for the mechanism fully opened position, an optical switch was introduced, and a protrusion was incorporated into the link AB to trigger the switch.

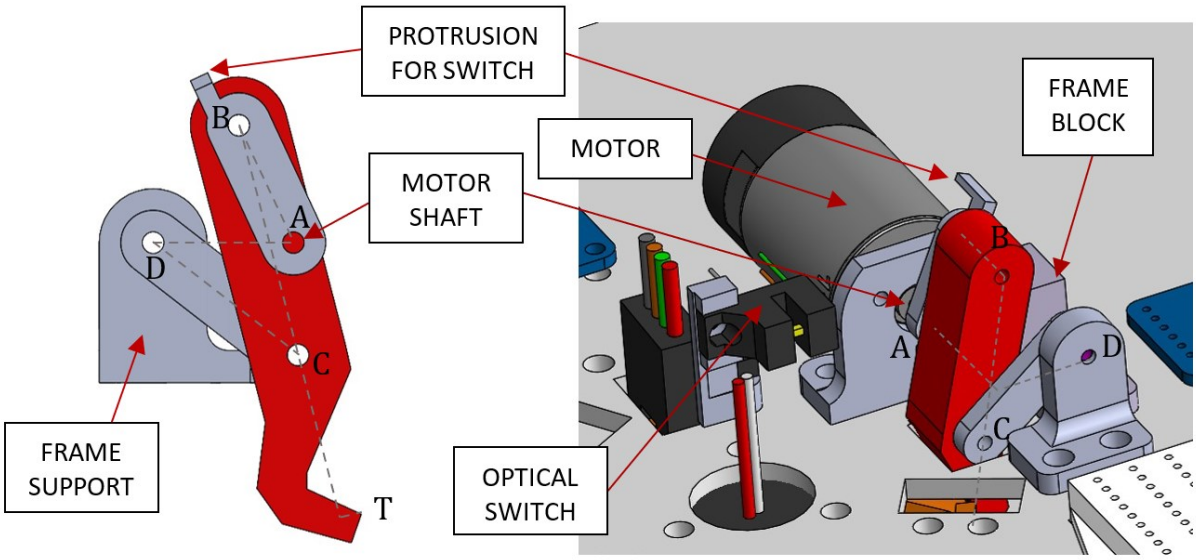

Figure 23: four-bar linkage final design.

6. Release Mechanism for Drogue Ejection

To overcome potential unlocking failures, such as those arising from motor malfunctions, a mechanism has been developed to be incorporated on the back of the drogue to eject it at a controlled direction and velocity in case of this occurrence.

6.1 Design Overview

The proposed mechanism involves Shape Memory Alloy (SMA) actuation to break a rigid connection between the drogue and the rest of the target, which is established via tie rod coupling. When actuated, the SMA imposes a tensile force to the tie rod, which is specifically designed with a notch to localize the desired fracture point. To expel the drogue away with a controlled velocity, the mechanism incorporates a preloaded elastic element. Additionally, a guide is required to move the ejected components through a precise trajectory. A schematic representation of the concept mechanism is depicted in *Figure 24*, while the detailed design and operating principle are further elaborated in the subsequent sections.

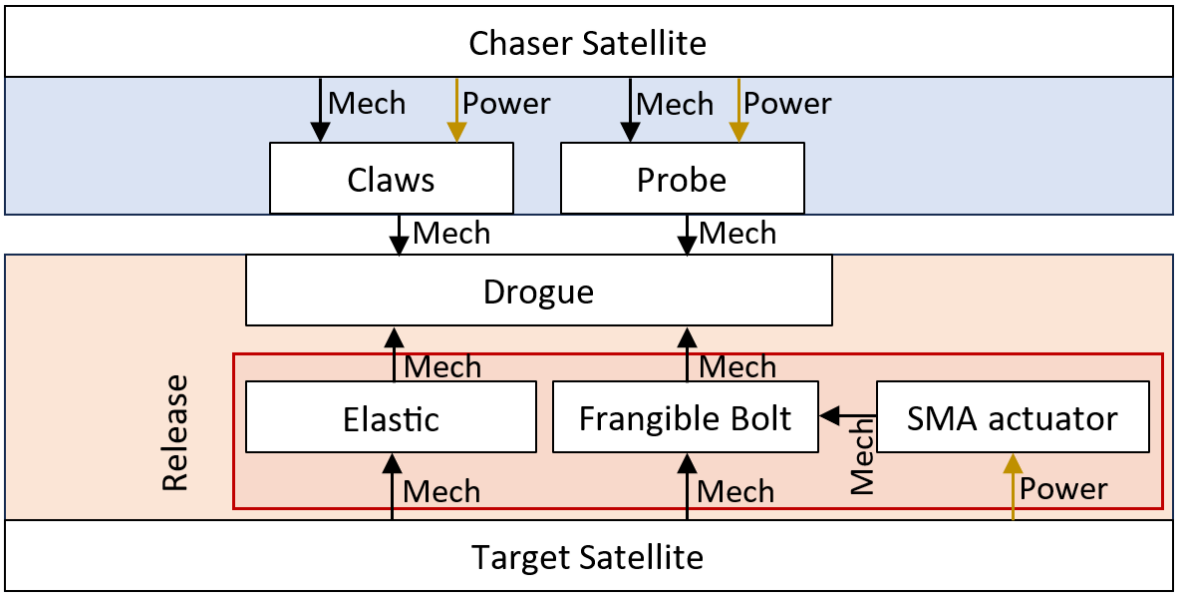

Figure 24: schematics of release mechanism.

6.2 Elastic element sizing

Some evaluations have been conducted to find the values of the spring rate and compressed length of the elastic element, matching the results with available off-the-shelf-components. The 12U chaser has been considered connected to the drogue and weighting 24kg. A desired escape velocity v_f was set at 10mm/s.

The compression length x_0 was initially set in the range between 1-10mm and the spring rate k was found consequently, based on the principle of energy conservation:

$$\frac{1}{2}k{x_0}^2 = \frac{1}{2}m{v_f}^2 \tag{37}$$

Where the elastic element is considered compressed at time $t = 0$ and at free length at $t = t_f$.

Knowing k, the natural frequency and the time to reach the free length are:

$$\omega = \sqrt{\frac{k}{m}} \tag{38}$$

$$t_f = \frac{\pi}{2\omega} \tag{39}$$

From these values, the three equations of motion for the ejected chaser-drogue assembly can be written:

$$x(t) = x_0 \cdot cos(\omega \cdot t + \varphi) \tag{40}$$

$$v(t) = -x_0 \cdot sin(\omega \cdot t + \varphi) \tag{41}$$

$$a(t) = -{x_0}^2 \cdot cos(\omega \cdot t + \varphi) \qquad (42)$$

To better visualize the results, a MATLAB script has been implemented and the resulting graphs are reported in *Figure 25*:

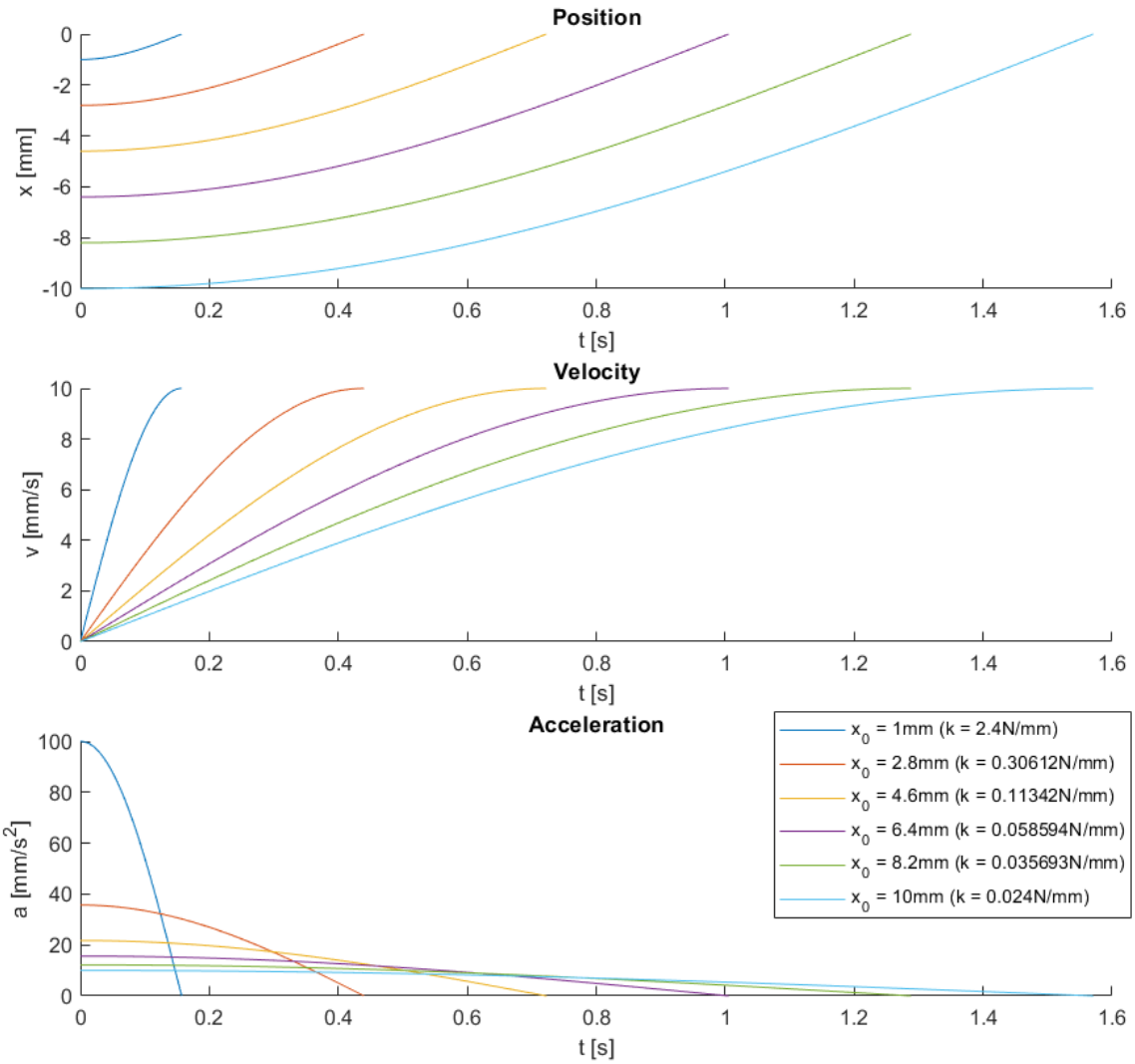

Figure 25: range of springs.

Following a first analysis of the results and comparing catalogues of springs from different sellers, the escape velocity has been raised at 20mm/s, due to the smallness of the spring rate or the compression length being too short. To give the ejected bodies a better aligned push, a wave spring has been preferred to a more

common cylindrical one, obtaining more contact surface and a bigger radius while keeping the length of the spring as short as possible. Maintaining the compression higher than 2mm and an outer diameter bigger than 10mm, very few components were available off-the-shelf. The chosen model is a wave spring with outer diameter of 12mm, inner one of 9mm, spring rate of 2.09N/mm and free length of 14.48mm.

With the selected model, to obtain a velocity of 20mm/s the spring is compressed of 2.14mm and the graphs are updated as in *Figure 26*. The spring imposes an acceleration of 190mm/s^2, 2% of the acceleration of gravity, which rapidly decreases as the time of total extension of the spring is around 1.7 milliseconds.

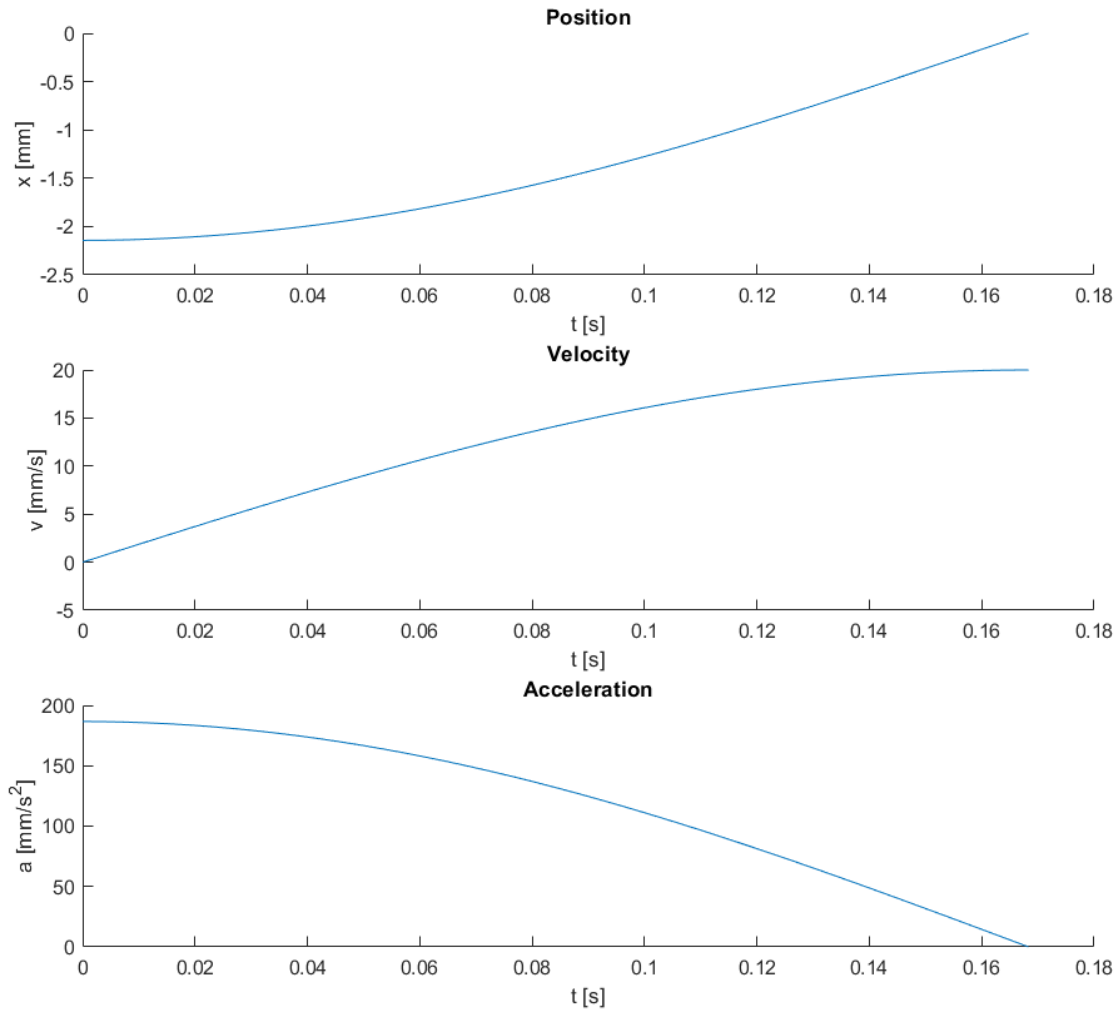

Figure 26: chosen spring performances.

6.3 Frangible bolt

The second part of the mechanism consists in a frangible dual threaded rod or bolt, specifically designed with a notch in the body which serves as a predetermined weak point, to localize the break. This element is then fastened through nuts or screwed in place after being surrounded by a cylindrical SMA actuator, which has been preloaded before. When the actuator is operated, it triggers the breakage of the bolt, which reaches fracture loads.

6.3.1 Rupture process

SMAs, such as NiTi, NiTiCu, CuAlNi and CuAlNiMn [38], possess a unique ability to return to a predefined shape or length when heated, allowing for controlled actuation. When preloaded, the SMA is mechanically compressed, increasing its potential energy. At occurrence, the SMA is heated through delivered power until it reaches the critical temperature for the Shape Memory Effect (SME) to take place. The SMA tries to return to its original shape and while doing so, it expands exerting a significant force which is harnessed to break the notched bolt. This force is controlled and predictable, offering a reliable means of actuation in the drogue ejection process.

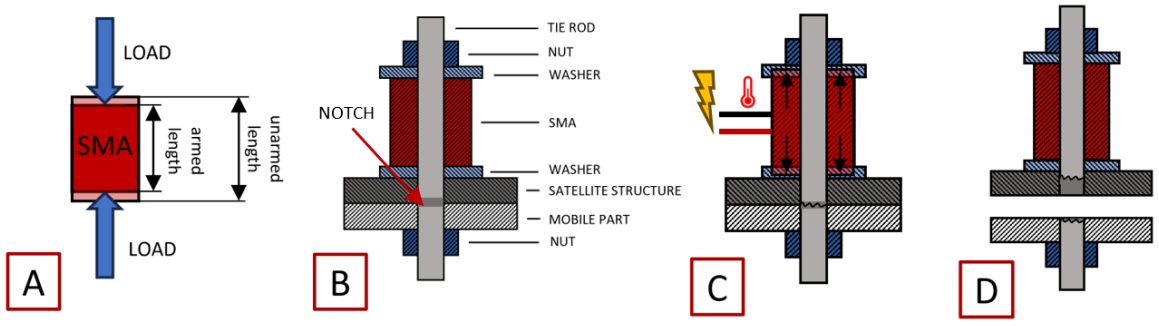

Figure 27: SMA actuator (A: actuator preloading process; B: actuator assembly; C-D: actuation and breakage of bolt through heating).

Usually, SMA are sold together with notched bolts and regarding the latter, there is generally a large variety of models or the option to request customized designs. After studying the compatible bolt size range from different SMA providers, the sizing of the frangible element can focus on the bolt itself.

For the size of its Triggy actuators, Nimesis has been considered as a valuable solution, including in its catalogue devices within the M2-M12 diameters range. For the frangible element, a dual threaded rod shape has been considered to connect both the drogue and the damper case, while housing the SMA actuator. The material of the available rods is Stainless Steel 15-5 PH with a fracture stress of 1300 N/mm^2.

6.3.2 Sizing

While the breakage is needed during the release of the drogue, the notched bolt must be sized to withstand the launch loads and the solicitations throughout the docking operations, because it is the connecting element between the drogue and the rest of the target satellite. To determine the appropriate frangible bolt size, the following considerations are made:

- **Docking Impact Loads:** The mass of the drogue (0.2 kg) and the satellite (24 kg) is factored in to evaluate launch loads. In a docking scenario with a non-damped impact at an expected velocity of 50mm/s, the estimated impact force is 242 N, assuming it as a fully elastic collision.
- **Launch Loads:** Considering the drogue as the sole component attached to the release mechanism (0.2kg) and as loads the ones impressed by a Vega C booster to its payload [39], the maximum experienced accelerations for the quasi-static loads are 5g in compression and 3g in tension. The forces experienced during the launch are then resulting in loads of 9.8 N (compression) and 5.8 N (tension).

With the calculated loads, an M2 bolt might already support the anticipated forces, having a fracture load of 454 N. However, to provide a safety margin and accommodate potential impulsive loads of 968 N, which is the case of a faster docking impact at 100mm/s, a minimum diameter of 3mm is suggested, which gives an extra protection, resisting up to 1021 N. The chosen SMA follows as a consequence of the diameter of the rod and consists of a TRHT03, capable of 3376 N of maximum preload, which details are presented in *Table 9*.

Material	Screw diameter (mm)	Max. preload (N)	Nominal power (W)	Outer diameter (mm)	Elongation (mm)	Armed length (mm)	Pulled length (mm)	Weight (g)
CuAlNi	M3	4689	4689	12	7.80	0.90	10.10	15.9

Table 9: datasheets of TRHT03.

The power required by the actuator is stated at 12W, requiring 7-8.4V or 14-16.8V to successfully activate the SMA by heating it at 163°C for approximately 60s. Since the system lays on the larger satellite, it should be a minor concern in terms of power consumption.

6.4 Proposed release mechanism design

To maintain a compact design, the entire mechanism is integrated around the tie rod, housing a single SMA actuator and a single wave spring acting as the elastic element. Knowing the armed length of the SMA actuator and considering proper washers, nuts and spacers, the proposed configuration of the drogue ejection mechanism is depicted as follows:

The release mechanism comprises an assembly concentric to the dual threads rod, arranged in the following order from bottom up as in *Figure 28*: a washer (grey), the SMA actuator (red), a second spacer (grey), and the compressed spring (dark

grey). The ferromagnetic plate (light grey) is connected to the drogue, featuring a concentric cylindrical guide to ensure the release motion aligns with the docking direction. The rod is threaded on the two sides to the guide plate and the damper, respectively. The dimensions of the considered system are 25.35 mm in length and 13 mm in diameter, which gives the necessary framework for integrating the solution into the existing structure.

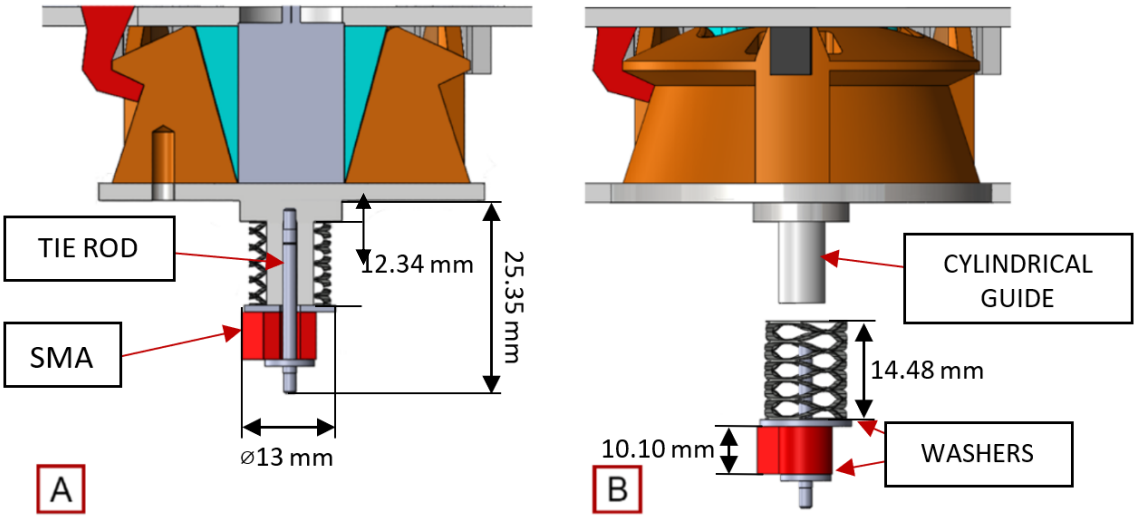

Figure 28: release mechanism final configuration (A: before actuation; B: after actuation).

7. Discussion of Results and Comprehensive Assessment

In the preceding chapters, the initial system was introduced, along with the objectives established for enhancing it and the process that led to the current model. This chapter will present the final system in its entirety, accompanied by a thorough comparison with the initial design. The assessment will evaluate the actual improvements in both functional and quantitative terms relative to the initial design. Considering the targeted refinement of specific aspects of the mechanism in this work, it is imperative to articulate the aspects that necessitate or allow further intervention. Moreover, it is essential to provide a detailed account of the limitations inherent in the results obtained to date.

7.1 Final design

As in the original design, the final iteration of the mechanism integrates three quadrilaterals actuated by stepper motors. Considered the selected model, Faulhaber AM2224, the motors have a step angle of 15° and each one is set to compute 8 full steps with the motor link AB of the four-bar mechanism rotating from the initial 0° position to the closure at 120° in respect of the satellite wall. As reported in *Figure 29*, the device is capable of pulling the drogue from within the last 3mm in docking direction with a force that increases from 3 N to 15 N with an angle of 65° from the horizontal x axis when the motor is providing a torque of 20 mNm. This means that the actuated four-bar linkage can eventually correct soft docking misclosures within the 3mm along the y axis, exerting at least 2.71 N along the docking direction and 1.27 N on the x axis. Considering the synchronous operation of the three linkages during the hard docking phase, it could potentially hold around 8N on the y axis, but further studies shall prove the actual capabilities in a three-dimensional scenario, involving also axial misalignment between the drogue and the probe.

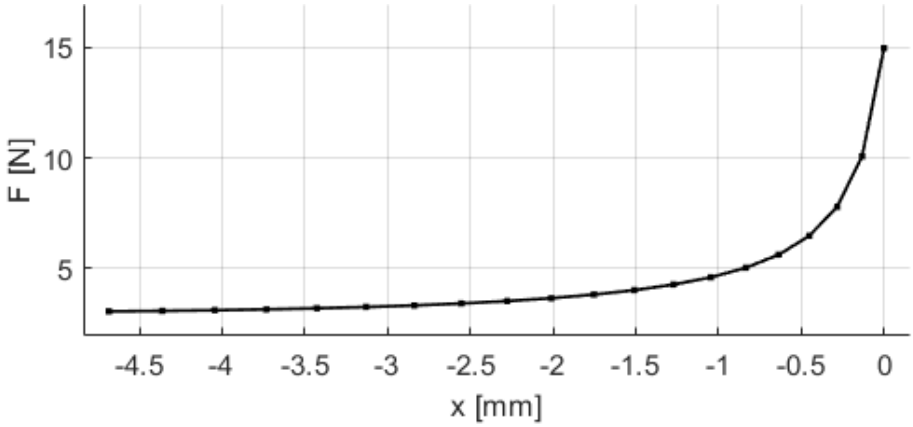

Figure 29: force of contact from y=-3mm to y=0mm.

At the end of the motion, when the claw is closed around the drogue, it is abutted to the frame transferring eventual drogue's loads in the negative y direction without further moving the mechanism. To open again the claws, a rotation in the opposite direction can be applied by the motors.

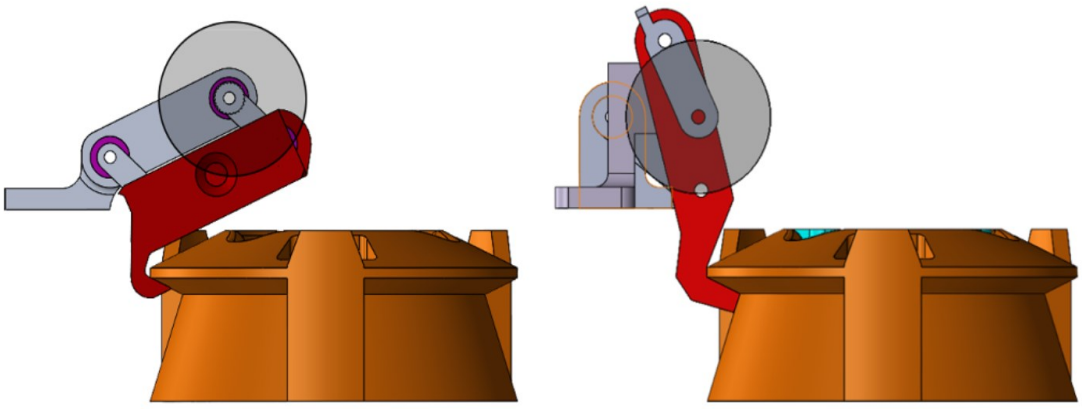

Figure 30: original and final versions of the four-bar mechanism at closure.

7.2 Comparison

Substantial modifications in the dimensions of the linkage, and consequently, the trajectory of the claw tip, made possible to develop a mechanism capable of holding the lock against external forces pulling the drogue along the negative vertical axis. In contrast, the initial design could only sustain a limited load on this axis without active actuators, relying solely the geometry of the mechanism and the intrinsic residual torque within the stepper motors.

This pivotal modification significantly enhances the energy efficiency and mechanical effectiveness of the mechanism, obviating the necessity for a more capable motor.

Across the various configurations studied during this thesis, the adjustments to quadrilateral components not only influenced the trajectory of the claw tip but also imparted a discernible impact on the output force exerted at the tip of the claw, obtained upon the motor torque. Through the study of kinematics and force analysis, it was observed that in the attempt to maximize the output force, configurations became progressively bulkier. To reach the desired locking capabilities of the final design, while obtaining a predominantly horizontal path of the claw tip, a compromise was reached, prioritizing the compactness of the system over the maximum achievable output force. In comparison to the initial mechanism, the trajectory obtained reduces of 1.7mm its maximum height, moving from 12.4mm from the chaser's plate to 10.7mm consequently remaining within the 24.5mm distance between the two plates. Meanwhile on the x-axis, the trajectory widens by 13.3mm from the original 29.7mm measured from the centre of the probe. With a fully opened mechanism distant 43mm from the centre of the probe, it provides increased clearance for drogue-probe coupling and mitigating the risk of interference or damage to the locking mechanism during the delicate mating operations. *Figure 31* gives an insight on the space and trajectory of original and final mechanism versions.

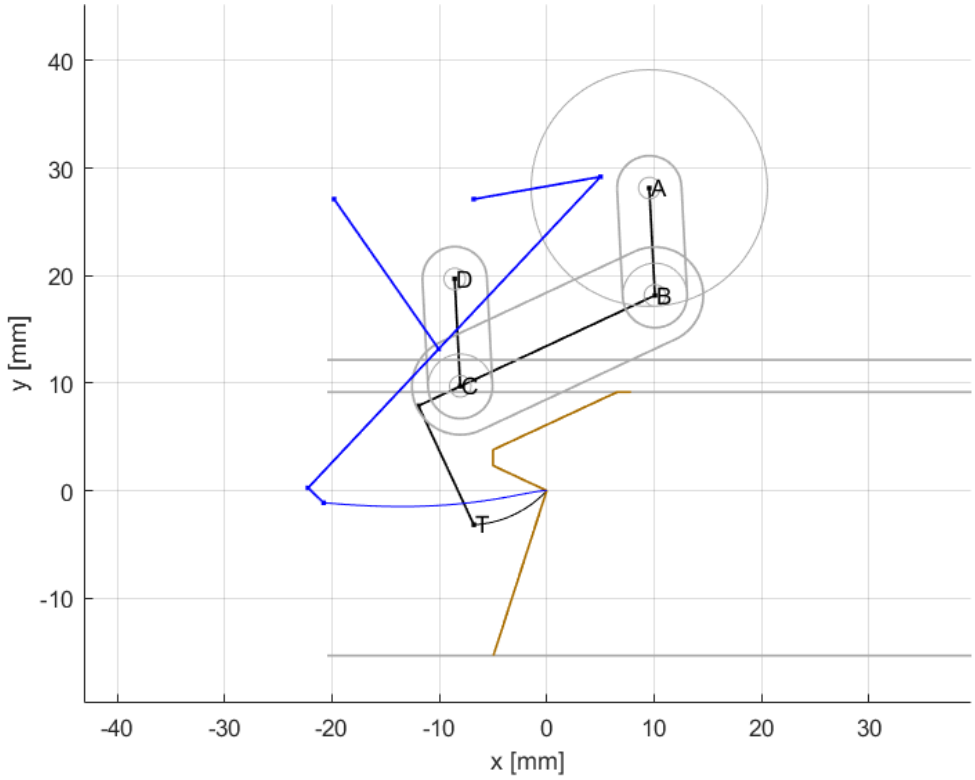

Figure 31: comparison of occupied spaces and trajectories between the original (black) and final (blue) versions of the mechanism.

It is noteworthy that while the final version of the mechanism improves the overall trajectory of the claw, it boasts a larger footprint on the inside of the chaser satellite than the original one as it is enclosed within a circle of diameter 126.8mm rather than the initial diameter of 100mm. Specifically, even though the mechanism itself has a slimmer profile, the motor is positioned farther from the centre of the drogue. This compromise is deemed acceptable in light of the functionalities acquired, and the prospect of further optimization is not precluded. Such optimization could potentially reduce the footprint even more, reverting it to within the desired 100mm diameter.

With regard to geometric tolerances and the precision required for manufacturing mechanism components, an evaluation has been conducted, noting that variations in the dimensions of the four links yield 0.5 to 2 times the displacement so, for an

error of +0.5mm in the length of link AB which may be caused by imprecisions in mounting ball bearing or in crafting the link AB itself, it results in a final position of the claw tip shifted of 1.26mm (0.95mm along X axis and 0.84mm along Y axis), while an error of -0.5mm on the same link length results on a shift of 1.3mm (1mm along X and 0.82mm along Y). While the aforementioned displacement is higher than standard machining for aluminium at around 0.13mm, which results in more manageable 0.33mm of tip shift if applied to the same link AB, combining different errors in the whole assembly could compromise the functionality of the mechanism. As an example, in *Figure 32* are reported the effects of length variation of ±0.13 for each single component.

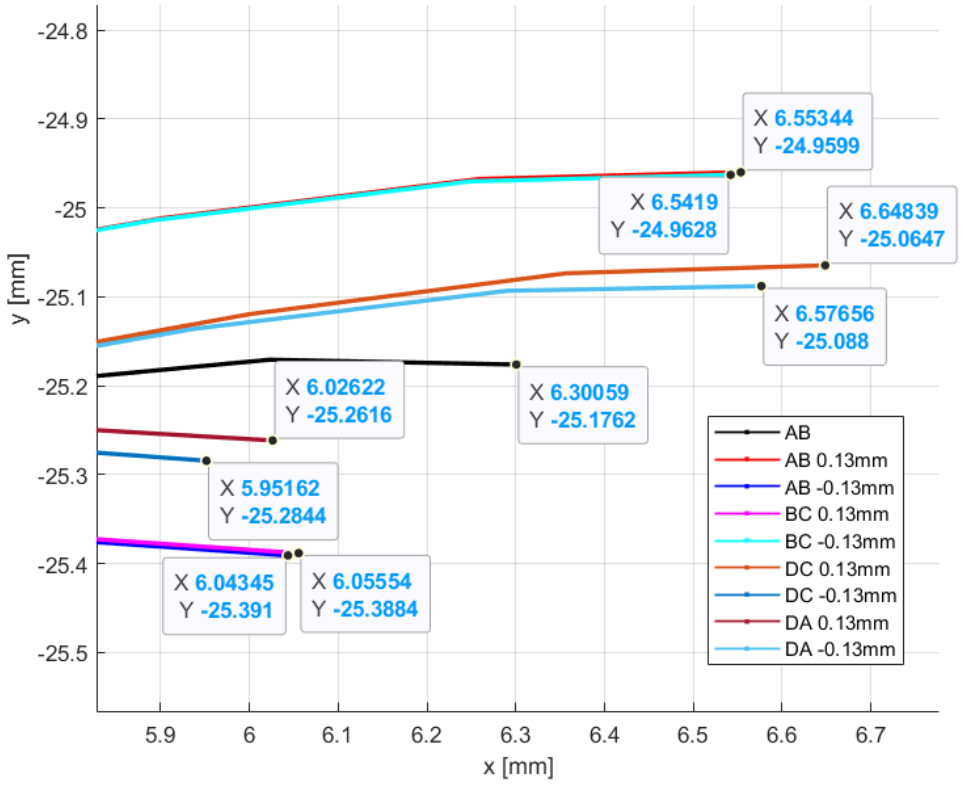

Figure 32: effects on the final position of the claw tip, given the machining tolerance of ±0.13mm for different links. In black without tolerances.

In particular, forces can drastically change in the nearby of toggle point. This means that with even a small amount of displacement, it is possible to reach very different results in term of output force module and direction. For this reason, it was chosen to remain $\Delta\theta_{AB} = 5°$ after the toggle position to avoid excessive solicitations to the joints and eventual misclosure.

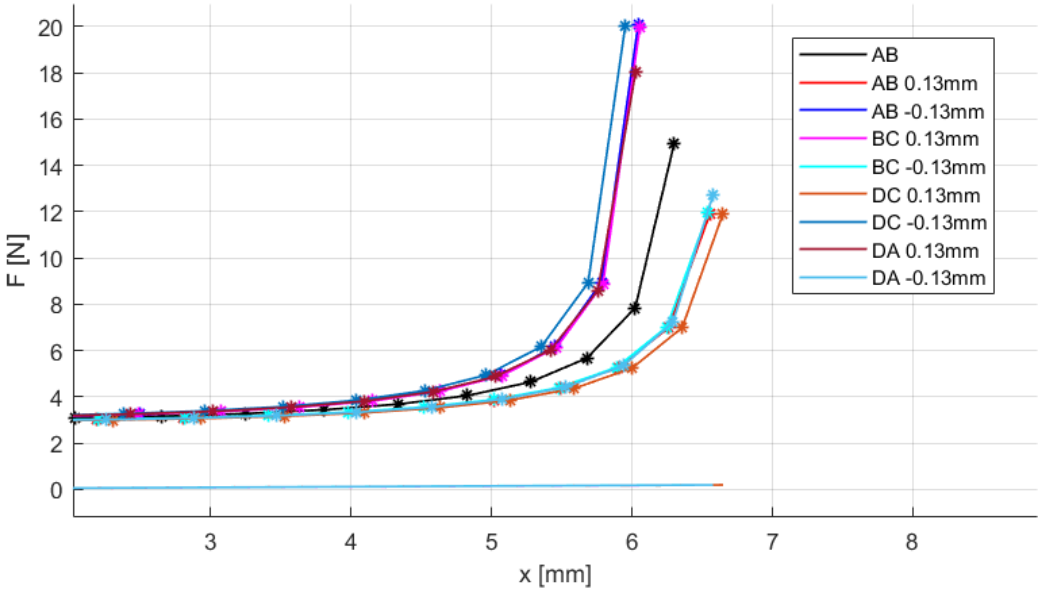

Figure 33: effects on the output force for a torque of 20mNm, given the machining tolerance of ±0.13mm for different links. In black without tolerances.

8. Conclusion and Future Work

This thesis focused on the hard-docking system of SROC, a future 12U CubeSat mission by the European Space Agency. The main requirement of the locking mechanism was to establish and sustain a rigid connection between the two interfaces of the docking system for small and microsatellites named DOCKS (DOCKS-A and DOCKS-B), developed by the University of Padova. Within this study, an iterative design process was employed to develop the four-bar mechanism used in the hard-docking procedure. Additionally, a release mechanism was incorporated to ensure undocking in case of a malfunction in the locking mechanism.

Chapter 1 served as an introduction to the work of this thesis, highlighting its objectives and structure, and presenting the state-of-the-art in docking solutions. In *Chapter 2*, docking procedures were described in more detail to provide context for the work developed in the following chapters.

Starting from *Chapter 3*, the original system was introduced and analysed, identifying possible areas of improvement to focus on. In this phase, it was crucial to identify the current availability of COTS to define the development limits of the actual system. Motors and joints were identified within this context to meet the constraints and requirements of the system. Specifically, finding a motor with consumption below 5W, remaining within spatial constraints, and producing useful torque (greater than 10mNm) proved to be a complex task.

Having assessed the capabilities and envelope of the available components, the next three chapters focused on modifying the mechanism. In *Chapters 4* and *5*, particular attention was given to the locking system, aiming to achieve a more effective closure capable of resisting even with the motor turned off and under strong loads pulling the drogue along the docking direction. Given the axial symmetry of the claws-drogue-probe-system, a two-dimensional implementation was adopted, focusing on a single linkage. This led to parallel mathematical modelling of the four-bar mechanism through kinematic and force analysis, implemented in

MATLAB, and the creation of a simulation using multibody software, specifically Working Model 2D, to compare the obtained results. This phase of the thesis proved to be the most complex as the iterative modification of the linkage required numerous adjustments, gradually leading to a deeper understanding of the system. The mathematical model used in force analysis aligned with observations in simulations, with the quadrilateral in a locked position under stationary conditions. Due to the rapid actuation of the mechanism by means of stepper motors (less than a second) without microstepping, significant impulsive loads could be generated, potentially influencing the hard-docking performance. Proper velocity profile will help in mitigating these effects.

As highlighted in the results discussion in *Chapter 7*, the goal of maintaining the mechanism passively locked was achieved, and the maximum force at closure was increased, considering the same input torque. Given the various areas of intervention, introducing the required innovations to obtain a mechanism that retains the compact qualities of the initial design has been notably challenging, leading to a compromise among different solutions. Consequently, the system's dimensions increased from an envelope of 100 mm to 127 mm.

In *Chapter 6*, the aim was to further enhance the system's functionalities by introducing a protection device against an eventual failure in opening the claws. A concept for a release mechanism was presented, involving a wave spring and SMA actuator, with a preliminary sizing and identification of the respective COTS components. The conducted study is still in the preliminary stages, and additional efforts may be directed towards a deeper understanding of the actuation process and the effects of screw breakage to ensure system reliability.

Lastly, in *Chapter 7*, the final design was compared with the initial one, and its performance was evaluated. To ensure full confirmation of the practicality of the proposed improvements, experimental validation will be essential. Physical proto-

types can be tested under controlled conditions, allowing the validation of simulated results and the identification of any unforeseen challenges. This iterative feedback loop between simulation and experimentation ensures a robust and reliable final design.

Based on the results obtained so far, it can be concluded that the work conducted in this thesis has increased the value of the docking system, enhancing locking capabilities and reducing power consumption. Through component analysis and modelling, a better characterization of the system has been provided, paving the way for the future developments mentioned throughout this chapter.

Bibliography

[1] A. Poghosyan and A. Golkar, "CubeSat evolution: Analyzing CubeSat capabilities for conducting science missions," *Progress in Aerospace Sciences,* vol. 88, pp. 59-83, 2017.

[2] F. L. de Sousa, "Are smallsats taking over bigsats for land Earth observation?," *Acta Astronautica,* vol. 213, p. 455/463, 2023.

[3] S. Wu, W. Chen, C. Cao, C. Zhang and Z. Mu, "A multiple-CubeSat constellation for integrated earth observation and marine/air traffic monitoring," *Advances in Space Research,* vol. 67, no. 11, pp. 3712-3724, 2021.

[4] B. Ygorra, F. Frappart, J. P. Wigneron, C. Moisy, T. Catry, B. Pillot, J. Courtalon, A. Kharlanova and S. Riazanoff, "ReCuSum: A polyvalent method to monitor tropical forest disturbances," *ISPRS Journal of Photogrammetry and Remote Sensing,* vol. 203, pp. 358-372, 2023.

[5] S. Janson, "2 - The concept and history of small satellites,," *Next Generation CubeSats and SmallSats,,* pp. 9-55, 2023.

[6] A. I. F. and A. Kak, "The Internet of Space Things/CubeSats: A ubiquitous cyber-physical system for the connected world," *Computer Networks,* vol. 150, pp. 134-149, 2019.

[7] V. Almonacid and L. Franck, "Extending the coverage of the internet of things with low-cost nanosatellite networks," *Acta Astronautica,* vol. 138, pp. 95-101, 2017.

[8] A. Flores-Abad, O. Ma, K. Pham and S. Ulrich, "A review of space robotics technologies for on-orbit servicing," *Progress in aerospace sciences,* vol. 68, pp. 1-26, 2014.

[9] R. Opromolla, G. Fasano, G. Rufino and M. Grassi, "A review of cooperative and uncooperative spacecraft pose determination techniques for close-proximity operations," 2017.

[10] W. A. N. G. Yongfang, Y. U. Xiaozhen and Y. U. Hang, "Research on autonomous on-orbit operation technology development based on patent analysis," *Flight Dynamics,* vol. 37, pp. 12-17, 2019.

[11] R. Foust, E. S. Lupu, Y. K. Nakka, S. J. Chung and F. Y. Hadaegh, "Ultra-Soft Electromagnetic Docking with Applications to In-Orbit Assembly," 2018. [Online]. Available: https://authors.library.caltech.edu/90231. [Accessed 4 11 2023].

[12] C. Saunders, D. Lobb, M. Sweeting and Y. Gao, "Building large telescopes in orbit using small satellites," *Acta Astronautica,* vol. 141, pp. 183-195, 2017.

[13] C. Underwood, S. Pellegrino, V. Lappas, C. Bridges and J. Baker, "Using CubeSat/micro-satellite technology to demonstrate the Autonomous Assembly of a Reconfigurable Space Telescope (AAReST)," in *Acta Astronautica, 114*, 2015.

[14] S. Eckersley, C. Saunders, D. Gooding, M. Sweeting, C. Whiting, M. Ferris, J. Friend, L. Forward, G. S. Aglietti, A. Nanjangud, P. C. Blacker, C. Underwood, C. P. Bridges and P. Bianco, "In-Orbit Assembly of Large Spacecraft Using Small Spacecraft and Innovative Technologies," 2018. [Online]. Available: http://epubs.surrey.ac.uk/849665. [Accessed 4 11 2023].

[15] C. Bonnal, J. M. Ruault and M. C. Desjean, "Active debris removal: Recent progress and current trends," *Acta Astronautica,* vol. 85, pp. 51-60, 2013.

[16] Z. B. L. X. H. A. J. P. H. G. S. &. W. S. Zhang, "An active removal method of space debris in geostationary orbit. Modern Electronics Technique," vol. 41, pp. 88-91, 2018.

[17] E. D. Rivera, P. Motaghedi and H. A. B., "Modeling and simulation of the Michigan Aerospace autonomous satellite docking system II," in *SPIE Defense + Commercial Sensing*, 2005.

[18] G. J. Wiens, A. Umsrithong, S. Miller, A. Koka and V. T., "Design of Autonomous Foldable Docking Mechanism for Small Space Vehicles," in *ASME 2009 International Design Engineering Technical Conferences and Computers and Information in Engineering Conference*, San Diego, California, USA, 2009.

[19] R. Krenn, K. Landzettel and R. Blommestijn, "Contact Dynamics Simulations for ConeXpress Docking Maneuvers," in *9th Int. Workshop on Simulation for European Space Programmes - SESP*, Noordwijk, Niederlande, 2006.

[20] R. Krenn, K. Landzettel and C. P. Kaiser, "Simulation of the Docking Phase for the Smart-OLEV Satellite Servicing Mission," in *9th International Symposium on Artificial Intelligence, Robotics and Automation in Space*, Los Angeles, USA, 2008.

[21] K. Ui, S. Matunaga and S. e. a. Satori, “Microgravity experiments of nano-satellite docking mechanism for final rendezvous approach and docking phase,” *Microgravity - Science and Technology,* vol. 17, p. 56–63, 2005.

[22] U. Kyoichi and M. Saburo, “Identification of Docking Possibility Criteria including Recovery from Incomplete Grasping of Docking Mechanism for Nanosatellite,” *Journal of Space Engineering,* vol. 2, no. 1, pp. 1-11, 2009.

[23] A. Boesso and A. Francesconi, “ARCADE small-scale docking mechanism for micro-satellites,” *Acta Astronautica,* vol. 86, pp. 77-87, 2013.

[24] M. Barbetta, A. Boesso and F. e. a. Branz, “ARCADE-R2 experiment on board BEXUS 17 stratospheric balloon,” *CEAS Space J,* vol. 7, p. 347–358, 2015.

[25] A. Caon, L. Lion, L. Olivieri, F. Branz and A. Francesconi, “Development of a smart docking system for small satellites,” in *Aeronautics and Astronautics - AIDAA XXVII International Congress*, 2023.

[26] J. Bowen, M. Villa and A. Williams, “Cubesat based rendezvous, proximity operations, and docking in the CPOD mission,” 2015.

[27] P. J. Tchoryk, A. Hays and J. Pavlich, “A docking solution for on-orbit satellite servicing: part of the responsive space equation,” in *AIAA-LA Section/SSTC*, 2001.

[28] L. Rodgers, N. Hoff, E. Jordan, M. Heiman and D. & Miller, “ A universal interface for modular spacecraft,” 2005.

[29] S. D. o. N. A. R. Corp. and N. M. S. Center, “Apollo Spacecraft News Reference,” 1972, p. 87.

[30] NASA, “Press Kit,” 1975.

[31] J. Pei, L. Murchison, A. BenShabat and V. Stewart, “Autonomous Rendezvous and Docking of Two 3U Cubesats Using a Novel Permanent-Magnet Docking Mechanism,” in *54th AIAA Aerospace Science Meeting*, 2016.

[32] M. C. R. M. M. T. F. V. F. V. M. .. &. F. A. Duzzi, “Electromagnetic position and attitude control for PACMAN experiment,” in *Proceedings of the 10th International ESA Conference on Guidance, Navigation & Control Systems*, Salzburg, Austria, 2017.

[33] ASI - Agenzia Spaziale Italiana, "ESA GSPT/Fly - SROC," [Online]. Available: https://www.asi.it/en/technologies-and-engineering/micro-and-nanosatellites/esa-gstp-fly-program/sroc/. [Accessed 7 11 2023].

[34] ESA, "Space Rider Overview," [Online]. Available: https://www.esa.int/Enabling_Support/Space_Transportation/Space_Rider_overview.

[35] S. Corpino, E. F. Stesina and A. Picerno, "Rendezvous manoeuvres of small satellites," 2023.

[36] M. Arredondo-Soto, E. Cuan-Urquizo and A. Gómez-Espinosa, "A Review on Tailoring Stiffness in Compliant Systems, via Removing Material: Cellular Materials and Topology Optimization," *Applied Sciences,* vol. 11, p. 3538, 2021.

[37] S. Linß, P. Gräser, T. Räder, S. Henning, R. Theska and L. Zentner, "Influence of geometric scaling on the elasto-kinematic properties of flexure hinges and compliant mechanisms," *Mechanism and Machine Theory,* vol. 125, pp. 220-239, 2018.

[38] S. Jayachandran, K. Akash, S. S. Mani Prabu, M. Manikandan, M. Muralidharan, A. Brolin and I. A. Palani, "Investigations on performance viability of NiTi, NiTiCu, CuAlNi and CuAlNiMn shape memory alloy/Kapton composite thin film for actuator application," *Composites Part B: Engineering,* vol. 176, no. 107182, 2019.

[39] "VEGA C User Manual," Arianespace, 2018. [Online]. Available: https://www.arianespace.com/wp-content/uploads/2018/07/Vega-C-user-manual-Issue-0-Revision-0_20180705.pdf.

[40] M. &. Simulink, "Space Rendezvous and Docking," MathWorks, [Online]. Available: https://it.mathworks.com/help/aeroblks/spacecraft-rendezvous-and-docking.html. [Accessed 7 11 2023].

[41] B. N. Dick, N. Mauch and T. Rupp, "Capture Latch Assembly for the NASA Docking System," in *44th Aerospace Mechanisms Symposium*, NASA Glenn Research Center, 2018.

[42] G. Aquino, "Design and verification of an adaptive control system for small satellites involved in rendez-vous and docking missions.," 2019. [Online]. Available: https://webthesis.biblio.polito.it/11237. [Accessed 4 11 2023].

[43] P. Pergola and V. Cipolla, “Mission architecture for Mars exploration based on small satellites and planetary drones,” 2016. [Online]. Available: https://emerald.com/insight/content/doi/10.1108/ijius-12-2015-0014/full/html. [Accessed 4 11 2023].

[44] L. Olivieri and A. Francesconi, “Design and test of a semiandrogynous docking mechanism for small satellites,” *Acta Astronautica,* vol. 122, pp. 219-230, 2016.

[45] Kulu, E., “Satellite Constellations - NewSpace Index,” 2016. [Online]. Available: https://www.newspace.im/. [Accessed 2023].

[46] S. Jackson, “NASA's CubeSat Launch Initiative,” 2017. [Online]. Available: https://nasa.gov/directorates/heo/home/cubesats_initiative. [Accessed 5 11 2023].

[47] E. Mabrouk, “What are SmallSats and CubeSats,” 2015. [Online]. Available: https://nasa.gov/content/what-are-smallsats-and-cubesats. [Accessed 4 11 2023].

[48] M. Ritter and D. Barnhart, “Geometry characterization of electroadhesion samples for spacecraft docking application,” 2017. [Online]. Available: https://ieeexplore.ieee.org/document/7943683. [Accessed 5 11 2023].

[49] X. Zhang, Y. Huang and X. Chen, “Analysis and design of parameters in soft docking of micro/small satellites,” *Science in China Series F: Information Sciences,* vol. 60, no. 5, p. 050204, 2017.

[50] A. Tsuiki, Y. Kawada and T. Hidaka, “Scenario on Orbital Experiment System using Small Satellites of NASDA,” 1993. [Online]. Available: https://digitalcommons.usu.edu/smallsat/1993/all1993/9. [Accessed 4 11 2023].

[51] D. Sellers, J. Rosenthal, V. Stewart, S. Elliott, J. Follman, M. N. Choueiri, P. Finch, M. Branchy, A. BenShabat, L. Murchison, J. Pei and R. Elandt, “Ground Demonstration on the Autonomous Docking of Two 3U CubeSats Using a Novel Permanent-Magnet Docking Mechanism,” 2017. [Online]. Available: https://ntrs.nasa.gov/search.jsp?r=20170001226. [Accessed 5 11 2023].